CT IMAGE QUALITY ASSESSMENT:

FROM PHANTOM DEVELOPMENT TO HUMAN OBSERVER STUDIES

By

Junyuan Li

A thesis submitted to Johns Hopkins University in conformity with the requirements for the degree of Master of Science in Engineering

Baltimore, Maryland

May 2020

Abstract

Purpose: To assess the Computed Tomography (CT) image quality by: first, developing custom phantoms with variable, controllable and repeatable texture features for the assessment of high-resolution CT scanners; second, applying the dynamic Fluence Field Modulation (FFM) technique and validating its efficacy by conducting a human observer study.

Methods: Procedural routines for texture generation were developed based on constrained sphere packing within specified volumes. Repeatability in phantom production was investigated by printing ensembles phantoms of the same design. They were scanned and registered for assessment of measures across different prints, permitting computation of standard deviation volumes and various radiomic measures to quantify variability. Tissue contrast control was achieved by immersing these phantoms in potassium phosphate solutions with varying concentrations.

Dynamic FFM was achieved by combining view-dependent Tube Current Modulation (TCM) and spatially modulating the X-ray beam through the Moiré patterns produced by the relative motion of Multiple Aperture Devices (MADs). Three different FFM imaging protocols were designed, and a 9 Alternative Forced Choice (9AFC) human observer study was to be conducted to evaluate their imaging performances.

Results: All texture inserts being developed exhibited great similarity with respect to the corresponding anatomical textures. The textures further depended on the 3D printer nozzle size: smaller nozzle resulted in higher printing quality and precision but with higher variability. Although biased from the ground truth, the low standard deviations of the radiomics and the standard deviation maps indicated high repeatability of the texture features. Results for the assessment of different FFM imaging protocols via the human observer study are ongoing pending Institutional Review Board (IRB) review.

Conclusion: The 3D printed texture phantoms offer a highly repeatable and flexible method to probe the ability of high-resolution CT to reproduce textures in reconstructed images. With increasing focus on task-based image quality and radiomics, such custom phantoms have the potential to play an increasing role in imaging performance assessments. The observer study with different FFM strategies helps to evaluate the detectability of certain texture features in CT scans. In summary, both the procedural phantom generation and the human observer study are effective methods for probing CT image quality.

THESIS COMMITTEE MEMBERS

J. Webster Stayman, Ph.D. (Advisor)
Associate Professor, Department of Biomedical Engineering
Johns Hopkins University

Wojciech Zbijewski, Ph.D.
Assistant Professor, Department of Biomedical Engineering
Johns Hopkins University

Grace J. Gang, Ph.D.
Assistant Research Professor, Department of Biomedical Engineering
Johns Hopkins University

ACKNOWLEDGEMENTS

I would like to express my gratitude to my advisor Dr. Webster Stayman, who guided me through the exploration of physics, engineering and design of the computer tomography system. His patience and insightful instruction always enlightened me to have new ideas and helped me getting through the difficulties throughout the problem-solving process. I also would like to thank to Dr. Grace Gang, who showed great patience and helped me solve problems many times.

I am also grateful to my colleagues in the AIAI and ISTAR lab, which are listed in alphabetical order: Michael Brahler, Qian Cao, Jessica Flores, Runze Han, Yixuan Huang, Andrew Leong, Stephen Liu, Shaoyan Pan, Niral Sheth, Amalie Shi, Gengxin Shi, Alejandro Sisniega, Shalini Subramanian, Matthew Tivnan, Wenying Wang, Pengwei Wu, Esme Zhang and Chumin Zhao. They always gave me helpful advices and willing to take their time to help me tackle with technical problems or to assist in my research.

Finally, I would like to thank Dr. Stayman, Dr. Gang and Dr. Zbijewski for supporting my research and willing to be my thesis committee members.

TABLE OF CONTENTS

Page

CHAPTER 1

CHAPTER 2

CHAPTER 3

LIST OF TABLES

Page

LIST OF FIGURES

Page

CHAPTER 1

1. General Introduction to Computed Tomography

Tomography refers to the cross-sectional imaging of an object from either transmission or reflection data collected by illuminating the object from many different directions [1]. This kind of visualization technique of patient anatomy differs from traditional 2D radiography by the capability of fully resolving the overlaying structure in the human body, which significantly helps the radiologists to diagnose disease. The basic mechanism of the Computed Tomography (CT) scanner is to take 1-D or 2-D projection data at certain steps in a full rotation (limited angle-of-view tomography is outside of the scope of this master thesis and will not be discussed), which are the measurements of the X-ray attenuation along the line between the X-ray source and the X-ray detectors. These projection data are then used to reconstruct the cross-sectional images. The introduction of the CT scanners is divided into 4 parts: first, we walk through several different CT scanning modes which are characterized by different scanning geometries; second, the basics of how X-ray interacts with objects and reconstruction methods for different scanning geometries are discussed; third, the common CT image quality assessments and CT system evaluation methods are introduced, as well as the need for novel, anthropomorphic phantoms; last, several different techniques of CT dose reduction are included.

1.1 Different geometries of CT scanners

There are several different scanning geometries for CT scanners, which include the parallel-beam, fan-beam and cone-beam geometries. Their working principles, applications as well as pros and cons are discussed in the following sub-sections.

1.1.1 Parallel-beam scanning geometry

The CT scanner adopting the parallel-beam scanning geometry is also called the First-generation (1G) CT scanner. It’s no longer manufactured for medical imaging, but its geometry is useful to understand and explain the theoretical ideas underlying image reconstruction. In short, the parallel-beam mode consists of 1) an X-ray source (whose X-ray beam has been collimated to a thin line; 2) a single detector moving in unison with the X-ray source along a linear path tangent to a circle which contains the object [2]. After one linear scanning, the X-ray source and the detector rotate to a new angle and repeated the previous process until a full rotation around the object is completed. The schematic of the parallel-beam geometry is as follows:

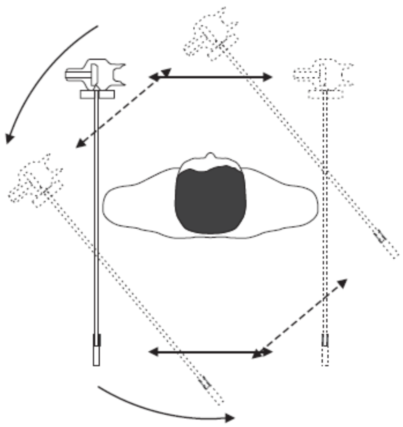

Figure 1: The parallel-beam geometry of the 1G CT scanner (Prince, 2015)

This kind of geometry has the following advantages: first, arbitrary number of rays from the X-ray source could be measured for a given projection at certain angle of view; second, due to the limited size of the detector, the scattering could be avoided to a large extent. However, the main drawback of the parallel-beam geometry is that the speed of data collection is too slow, thus making it almost impractical for clinical use.

1.1.2 Fan-beam geometry

The improvement over the 1G CT scanner leads to the fan-beam geometry, where a fan-beam covers the entire object with the X-ray source held in a single position. One of its most representative application is the third-generation (3G) CT scanner, which is shown below:

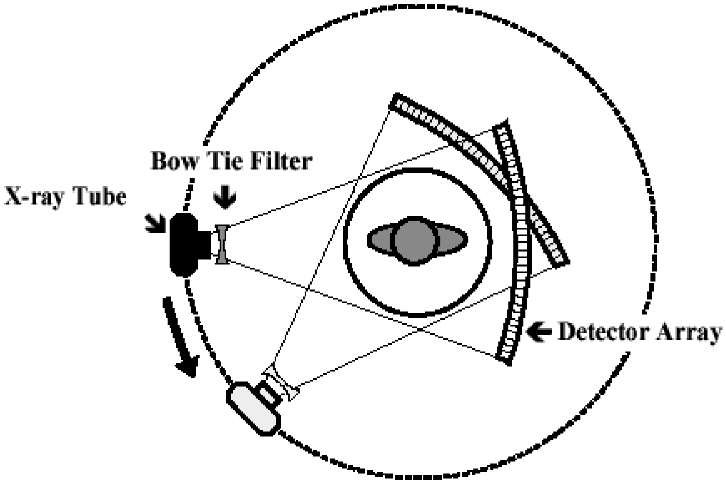

Figure 2: The fan-beam geometry of the 3G CT scanner (KieranMaher at English Wikibooks, 2006)

For each angle of view, the X-ray source and the detector no longer need to move linearly in unison; rather, now they just need to rotate in synchronization during the scan. The advantages of the 3G CT scanner include: first, a dramatic decrease in scan time compared to the parallel-beam case. A typical 3G scanner acquires 1,000 projections with a fan-beam angle of 30-60 degrees incident upon 500-700 detectors within 1-20 seconds. Second, the relatively simple rotational motion of the X-ray source and the detector and the highly parallel detection capability. The disadvantages include the relatively high cost due to the manufacturing of a large number of detectors and scattering artifacts even if the X-ray beam has been collimated [3].

1.1.3 Cone-beam geometry

So far, the parallel-beam and fan-beam geometry of the previously described CT scanners focus on 1-D projections corresponding to 2-D reconstruction and only a single slice of the object. Cone-beam geometry, in short, is a generalization and extension of fan-beam geometry in 3-D space and enables the capability of volumetric reconstruction, which makes the process of data-collection much more efficient. The geometry setup of the cone-beam CT scanner with the planar detector may be visualized as follows:

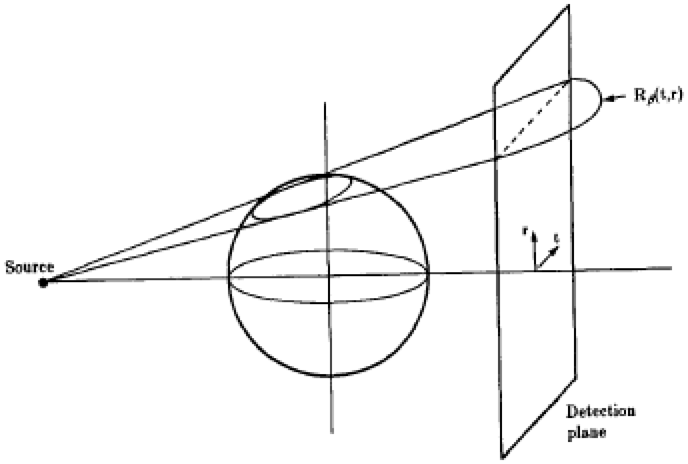

Figure 3: The geometry of the cone-beam CT scanner (Kak, Avinash C., and Malcolm Slaney,2001)

Instead of illuminating a slice of the object with the 2-D fan-beam pattern, now the entire object is illuminated with a point X-ray source and the X-ray flux is measured on a planar detector. The main advantages of this scanning geometry include the high efficiency of data collection and volumetric reconstruction (instead of a single cross-sectional image of the object, now multiple slices of the object are reconstructed at the same time); but the trade-off are more severe scattering artifacts due to the large area of the planar detector. Other potential drawbacks include those associated with the flat-panel detector technology used for CBCT due to panel size and detector nonidealities like detector glare and readout speed.

1.2 CT Reconstruction Algorithms

In this section, the basic reconstruction algorithm and how it is generalized and extended from parallel-beam to fan-beam and to cone-beam will be discussed in detail. In addition to analytical solutions, we will describe statistical reconstruction algorithms which incorporate the prior information about the object and a statistical model which improves the image quality – dose trade-off.

1.2.1 Beer's Law

Beer's Law describes fundamentally how the X-ray beam is attenuated by the object and serves as a model at the projection data:

$$I = I_0 \int S(E) e^{-\int \mu(\vec{x};E)dl} dE \qquad (1)$$

Where: I is the measured X-ray photon fluence (projection data)

I_0 is the bare-beam fluence

$\mu(x, y; E)$ is the attenuation coefficient of the object at location $\vec{x}$ and energy level E

$S(E)$ is the detector response at energy level E

It's also called the *fundamental photon attenuation law*. This equation is typically simplified to the monoenergetic case, wherein Eq (1) reduces to:

$$I = I_0 e^{-\int \mu(\vec{x}) dl} \qquad (2)$$

Which is the most common model for simple CT projection data formation and reconstruction theories.

1.2.2 Parallel-beam geometry

As stated above, projection data can be approximated by line integrals. For the purpose of computational implementation, Eq (2) should be discretized, which calls for the parameterization of the object as in Figure 4:

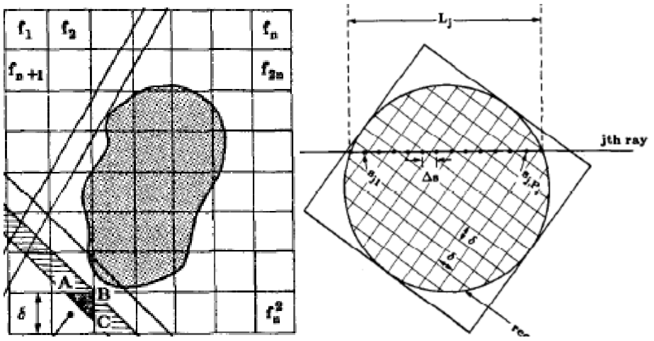

Figure 4: Parameterization of the object and discretization of the line integral (Kak, Avinash C., and Malcolm Slaney,2001)

In short, the continuous-domain object is now divided into discretized grids inside a bounding box, where each voxel corresponds to the path-length passed by the light ray. Assuming there are p pixels after object parameterization, the measurement on the i^{th} detector may be expressed as the discrete form of Eq (2):

$$\overline{y_i} = I_0 exp\left(-\sum_{j=1}^{p} a_{ij}\mu_j\right) + I_b \qquad (3)$$

Where: a_{ij} represents the path-length corresponding to the i^{th} detector in the j^{th} pixel

μ_j represents the attenuation coefficient for the j^{th} pixel

I_b represents the offset of the measurement

Collecting all a_{ij} into a system matrix A and vectorizing the map of attenuation coefficients μ**,** the projection at each angle may be expressed in a more compact form [4]:

$$\overline{\boldsymbol{y}} = I_0 exp(-\boldsymbol{A\mu}) + I_b \qquad (4)$$

After data collection, the image is to be reconstructed from these projection measurements. Analytic reconstruction is most easily introduced in the 2-D parallel-beam case. The Fourier Slice Theorem states that the 1-D Fourier transform of the projection data, $P_\theta(t)$, is equal to the slice of 2-D Fourier transform of the entire image $\mu(x, y)$ to be reconstructed, which is mathematically expressed as follows [5]:

$$S_\theta(w) = F(w, \theta) = F(w \cdot cos\theta\,, w \cdot sin\theta) \qquad (5)$$

Where: $S_\theta(w) = \int_{-\infty}^{+\infty} P_\theta(t) e^{-j2\pi wt}\, dt$

$F(u, v) = \int_{-\infty}^{+\infty} \int_{-\infty}^{+\infty} f(x, y) e^{-j2\pi(ux+vy)} dx\, dy$

The following figure visually illustrates this idea:

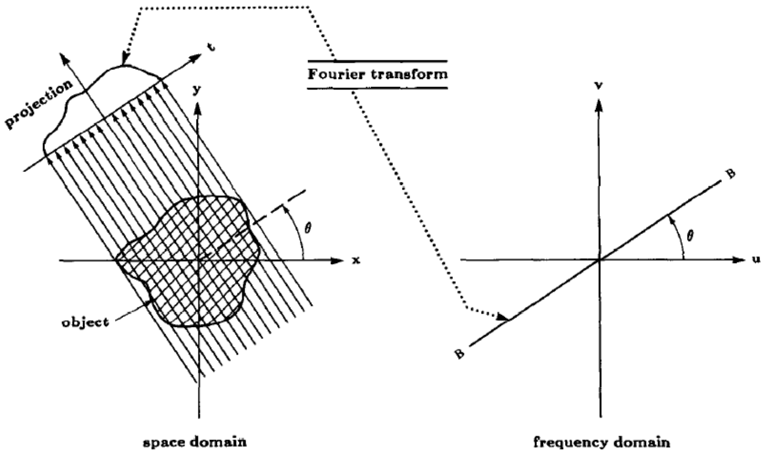

Figure 5: Pictorial illustration of the Fourier Slice Theorem (Kak, Avinash C., and Malcolm Slaney,2001)

This theorem directly paves the way to image reconstruction:

$$f(x,y)=\int_{-\infty}^{+\infty}\int_{-\infty}^{+\infty}F(u,v)e^{-j2\pi(ux+vy)}du\,dv \qquad (6)$$

Combined with the substitutions: $u = w \cdot cos\theta,\ v = w \cdot sin\theta,\ dudv = wdwd\theta$ and Eq (6), the reconstruction formula becomes:

$$f(x,y)=\int_{0}^{\pi}\int_{-\infty}^{+\infty}S_{\theta}(w)|w|e^{j2\pi wt}dw\,d\theta \qquad (7)$$

Notice that the term $|w|$ is a ramp filter in the spatial frequency domain. Eq (7) introduces a classical way of image reconstruction, which is called Filtered Back-projection (FBP). It is an algorithm that can be used to reconstruct an image from projection measurements. Practically, the reconstruction steps are as follows:

1) After gain and offset correction, take negative logarithm to obtain an approximation of the line integral $A\mu$ at each angle and forms the sinogram.

2) Apply the ramp filter to the line integral to counteract the $1/r$ blur in the reconstructed image that results from back-projection alone.
3) Back-project the line integral at each angle along the rays. While the above reconstruction steps were originally prescribed for parallel projections, the same basic process can be extended to other geometries.

1.2.3 Fan-beam geometry

For a fan-beam geometry, FBP has a similar form. We parameterize the ray equation by angle $\beta \text{ and } \theta$, change the image coordinates from Cartesian to Polar coordinate system and put a "virtual detector" across the center of parameterized object. This is illustrated in Figure 6:

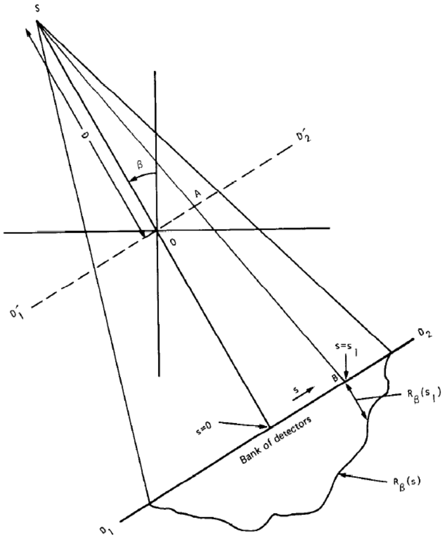

Figure 6: The fan-beam geometry for image reconstruction (Kak, Avinash C., and Malcolm Slaney,2001)

The fan-beam reconstruction follows the same three steps as in the parallel-beam case but with additional fan-beam geometrical weighting:

1) Apply the cosine-weighting to the projection data at each angle of view, which is based on the deviation of the X-ray beam from the center line of the X-ray.

2) Perform modified ramp filtering similar to the parallel-beam case.
3) Apply the fan-beam geometrical weighting to the ramp-filtered projection data and integrate them view by view.

1.2.4 Cone-beam geometry

The cone-beam geometry is a generalization of the fan-beam geometry; in each view, the cone-beam projection data may be viewed as being composed of a set of tilted fan-beam projections which is shown as follows:

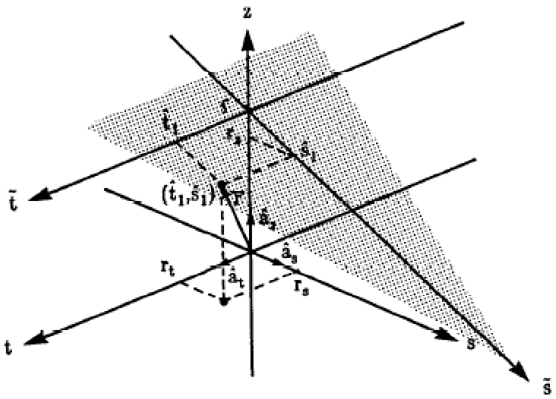

Figure 7: The cone-beam scanning geometry (Kak, Avinash C., and Malcolm Slaney,2001)

In summary, the reconstruction is based on filtering and backprojecting in a single plane within the cone. At each angle of view, each elevation on the detector coordinate is considered separately and the final 3-D reconstruction is obtained by summing the contribution to the object from the corresponding tilted fan-beam projections [6]. Thus we may reconstruct the entire object by following exactly the same procedure as in the fan-beam case, only with the difference in modified cosine-weighting and cone-beam weighting terms.

1.2.5 Likelihood-based Reconstruction Algorithm

In contrast to the analytic FBP reconstruction algorithm, there are implicitly derived approaches that seek to iteratively update the attenuation coefficients map (the discretized object function) according to some objective functions. For example, likelihood-based objective function seeks to maximize the probability that projections of the object estimate match the real measurements. For the object being parameterized as in Figure 4, the maximum-likelihood (ML) estimate for the object function $\hat{\boldsymbol{\mu}}$ is defined as follows:

$$\hat{\boldsymbol{\mu}} = {}^{argmax}_{\mu \geq 0} L(\boldsymbol{\mu}; \boldsymbol{y}), \quad L(\boldsymbol{\mu}; \boldsymbol{y}) = logP[\boldsymbol{Y} = \boldsymbol{y}; \boldsymbol{\mu}] \qquad (8)$$

Where: $\boldsymbol{\mu}$ is the vector of attenuation coefficients:

$\boldsymbol{Y}$ is the mean model of projection data described in Eq (4)

$\boldsymbol{y}$ is the measured projection data

If we apply the Poisson model to describe the quantum noise associated with X-ray photon generation, the measurement joint probability mass function is as follows:

$$P[\boldsymbol{Y} = \boldsymbol{y}; \boldsymbol{\mu}] = \prod_{i=1}^{N_Y} P[Y_i = y_i; \boldsymbol{\mu}] = \prod_{i=1}^{N_Y} \frac{e^{-\bar{y}_i(\boldsymbol{\mu})}[\bar{y}_i(\boldsymbol{\mu})]^{y_i}}{y_i!} \qquad (9)$$

Studies have shown that maximizing the log-likelihood in Eq (8) results in unacceptably noisy images. This is because tomographic image reconstruction is an ill-conditioned problem, meaning that there are many possible choices of the parameterized object function $\hat{\boldsymbol{\mu}}$ which fit the real measurements $\{Y_i\}_{i=1}^{N_Y}$ reasonably well, when the fit is quantified only by the log-likelihood $L(\boldsymbol{\mu})$ [7]. To tackle this problem, we could modify the objective function $L(\boldsymbol{\mu})$ by incorporating a penalty term, as in follows:

$$\hat{\boldsymbol{\mu}} = {}^{argmax}_{\mu \geq 0} \phi(\boldsymbol{\mu}; \boldsymbol{y}), \quad \phi(\boldsymbol{\mu}; \boldsymbol{y}) = L(\boldsymbol{\mu}; \boldsymbol{y}) - \beta R(\boldsymbol{\mu}) \qquad (10)$$

$$R(\boldsymbol{\mu}) = \sum_{j=1}^{N_P} \frac{1}{2} \sum_{k=1}^{N_P} \omega_{jk} \varphi(\mu_j - \mu_k) \qquad (11)$$

Where $R(\boldsymbol{\mu})$ describes a penalty between neighboring voxels and allows us to enforce desirable object properties or prior information about the object, such as piece-wise constant or piece-wise smooth image properties. This penalty term permits control of the tradeoff between noise reduction and spatial resolution and eliminates ambiguity between the many possible solutions in the ill-conditioned problem.

By optimizing the modified objective function which incorporates the penalty term, the Penalized-Likelihood (PL) approach can work well for low-dose CT scans. Highly-parallelized algorithms, such as Separable Paraboloidal Surrogate (SPS) algorithm have been proposed by Erdogan [8] and Wang *et al* [9] to facilitate the reconstruction process with the help of CUDA tools and advanced GPU hardware.

1.3 Enhancement of CT image quality by modifying X-ray fluence distribution

During a CT scan, X-ray photons generally cover a relatively large portion of the patient's body and a significant portion of x-ray photons are attenuated as deposit energy in human tissues. This results in a two-fold problem: first, if X-ray coverage is more than needed, the patients will receive more radiation dose with potential harm to their bodies. Second, due to the heterogeneity of human anatomical structure, different numbers of X-ray photons will come out at different positions of the patients, which might deteriorate the CT image quality due to the limited dynamic range of the detector. For example, given a homogeneous X-ray spatial distribution, the number of X-ray photons exiting along line integrals with thicker parts of the patient will be much less than that of the photons exiting from thinner parts of the patient because of the higher attenuation. Thus, there is the potential for inadequate signal strength for thicker parts and excessive signal for thinner parts of the patient, resulting in inefficient x-ray usage; that is, exposure requirements may be driven by its most attenuating regions. To overcome this clinical difficulty, the following are common practices: X-ray beam shaping and Tube Current Modulation (TCM).

X-ray beam shaping is typically accomplished by using an x-ray collimator and a compensational filter. The collimator has flexible mechanical design which consists of several pieces of lead capable of completely blocking the X-ray outside of the region of interest. But this confinement of X-ray spatial distribution is largely binary and fails to consider the heterogeneity inside the human body. To further address this problem, we use the compensational filter in addition to the collimator, which blocks X-ray photons according to relative thickness in the object being imaged. For instance, as shown below, these compensational filters block more X-ray photons at the thicker part of the human body than at the thinner parts, thus providing enough signals for the high-attenuation part and preventing excessive x-ray exposure for the less-attenuating part. These filters are so-called bow-tie filters (due to their shape) and are common in clinical CT.

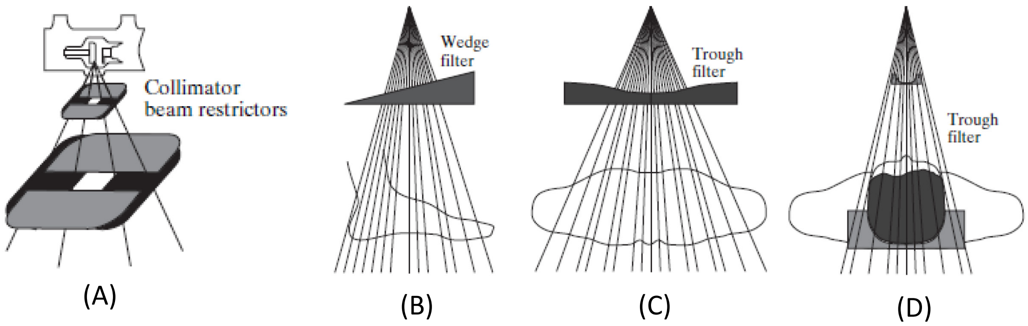

Figure 8: Collimators and filters used for modulation of x-ray fluence distribution. (A) Commonly-seen collimator in a CT scanner (Prince, 2015) (B)(C)(D) Various compensational filters (Prince, 2015)

The other strategy, TCM (or sometimes called Automatic Exposure Control, AEC), provides a different way of adjusting the number of X-ray photons with regard to different object thicknesses. Instead of using physical filters to block the incoming X-ray photons, one may adjust the tube current in the X-ray source to control the number of overall X-ray photons interacting with the human body in a view-by-view fashion. During the scan, when the X-ray source rotates to a view with high overall attenuation, it increases the tube current. Alternately, lower tube current is applied for the low overall attenuation case. A pictorial illustration of TCM is shown in the following:

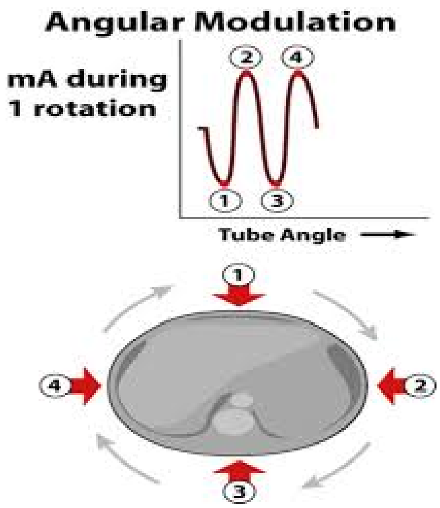

Figure 9: TCM workflow during one rotation (Azmardi, 2015)

Modern clinical CT systems employ one or more static bowtie filters to accommodate patient shape. In research settings, more advanced dynamic bowtie filters have been developed that permit a changing beam profile during a CT acquisition. These strategies may be used in combination with TCM to permit greater flexibility of X-ray beam modulation, thus achieving more effective dose distribution, lowering the overall radiation dose and acquiring desired image qualities.

1.4 CT image quality assessment

Traditional methods for CT image quality assessment, including the computation of spatial resolution and noise, are often characterized by Modulation Transfer Function (MTF), noise power spectrum (NPS) and contrast-to-noise ratio (CNR). However, CT image quality assessments are increasingly quantified using task-based performance metrics. Such analysis has often focused on elements including detectability of lesions and discrimination of lesion types, which results in another metric for assessment of CT image quality: the detectability index. The detectability index describes the ability to perform specific tasks like lesion detection. Various model observers have been proposed to formulate the detectability index and accordingly optimize the CT system performance, such as the Channelized Hotel Observer (CHO) and Non-prewhitening Observer (NPW). Ultimately, the gold standard for CT system evaluation is to perform a human observer study wherein an imaging task is tested directly. However, such studies are time consuming and can be expensive and difficult to perform.

In the context of the emerging radiomic analysis, it becomes important to assess image quality in terms of performance in assessment of textural biomarkers. Radiomics involves the high-throughput extraction of quantitative imaging features with the intent of creating mineable databases from radiological images [10]. One class of radiomic measures is based on the Gray Level Co-occurrence Matrix (GLCM). Scalar metrics computed from the GLCM can describe features in terms of autocorrelation, contrast, dissimilarity, etc. These texture features have found importance in many areas including diagnostics based on heterogeneity of lesions; the repeatability of texture features can also serve as a metric of image quality assessment.

Many factors can influence the appearance of texture in a CT image volume including reconstruction and data processing (especially advanced reconstruction methods like model-based reconstruction and machine learning methods due to their nonlinear nature). Image properties vary from system to system, with new high spatial resolution scanners that permit visualization of finer anatomical features. We seek to develop methods to probe the ability of a CT system to reliably reproduce specific textures by producing phantoms (or phantom inserts) with variable, controllable, and repeatable textures. Such test objects provide custom texture features for evaluation of geometric measurements of the microarchitecture.

CHAPTER 2

2. ANTHROPOMORPHIC PHANTOM DEVELOPMENT FOR CT SYSTEM ASSESSMENT

2.1 BACKGROUND & MOTIVATION

Imaging phantoms are specially designed objects in the field of medical imaging to evaluate image quality or help perform geometrical calibration for a variety of medical imaging devices such as CT, Ultrasound and Magnetic Resonance Imaging (MRI). They provide us with consistent structures within the object being imaged to help us investigate the imaging performance of the devices, without using living objects to avoid changing structures and direct radiation exposure. In the field of CT imaging, there exist two main forms of imaging phantoms: computational phantoms and physical phantoms.

Computational human phantoms are mathematical models used in computer analysis and simulation of a CT scanner. One popular computational phantom is the Shepp-Logan (S-L) phantom, which consists of ten ellipses with different geometrical parameters and gray levels. It is intended to simulate the human brain and serves as a standard image to evaluate and compare different CT image reconstruction algorithms. However, with the rapid development of advanced CT scanners in the market, the oversimplified Shepp-Logan phantom fails to represent many more complex and important human anatomical structures. Since the development of the S-L phantom, computational phantoms have underwent the following three generations: first generation, the stylized computational phantoms; second generation, the voxelized phantoms; and the third generation, Boundary Representation (BREP) phantoms.

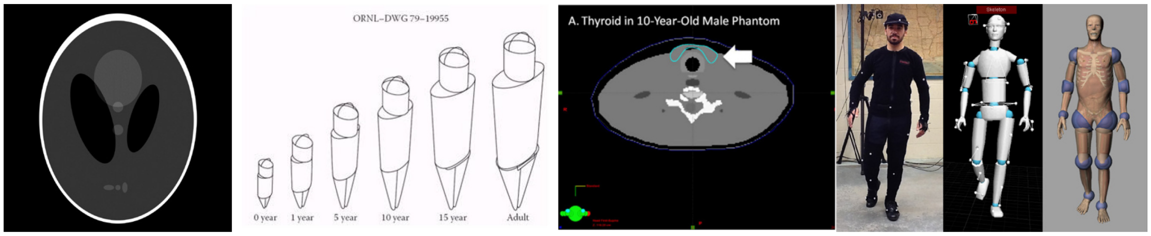

(A) (B) (C) (D)

Figure 10: The evolution of computational phantoms. (A) Shepp-Logan phantom (B) Stylized computational phantom (Kramer,2004) (C) Voxel computational phantom (Lee, 2015) (D) BREP phantom (Xu, 2005)

The stylized phantom is a mathematical representation of the human body which, when coupled with a Monte Carlo radiation transport computer code, can be used to track the radiation interactions and energy deposition in the body [11]. It models the human body with a set of more complex geometrical shapes and customizable parameters, but still suffers from oversimplification. Voxelized phantoms were developed by combining diagnostic images produced by high-resolution CT scanners and converting them into 3D volumetric models. This innovation significantly enhanced the accuracy of the computational phantom, but was limited by extremely high memory requirements. Finally, BREP phantoms are based on polygonal meshes and contain both exterior and interior anatomical features of the human body, pushing the limit of phantom accuracy even higher [12].Although computational phantom have become more sophisticated and CT simulations more complex, physical phantom testing is often the only way to be sure all important physical effects are studied. This is particularly true for newer systems for which simulation models are incomplete or where data processing steps are proprietary or “black box” modules.

Physical phantoms are composed of materials with the similar attenuation coefficients as those in the human body. Many phantoms lack complex anthropomorphic textures or structures since traditional image quality assessment has focused on spatial resolution, attenuation quantification, or noise estimation in uniform regions. As shown below, a spatial resolution phantom is made of uniform polymethyl methacrylate (PMMA) material with a series of metal line pairs inserted. Such a phantom serves for the purposes of resolution characterization and image quality assurance. By comparing and inspecting the visibility of each line pair pattern, one can evaluate the spatial resolution property of the system; by selecting the homogeneous area and computing the NPS, we investigate the reconstructed noise level and the degree of isotropy of the system. With the advancement in spectral CT, phantoms made with multiple homogeneous materials with different attenuation coefficients are used to evaluate the image quality after material decomposition.

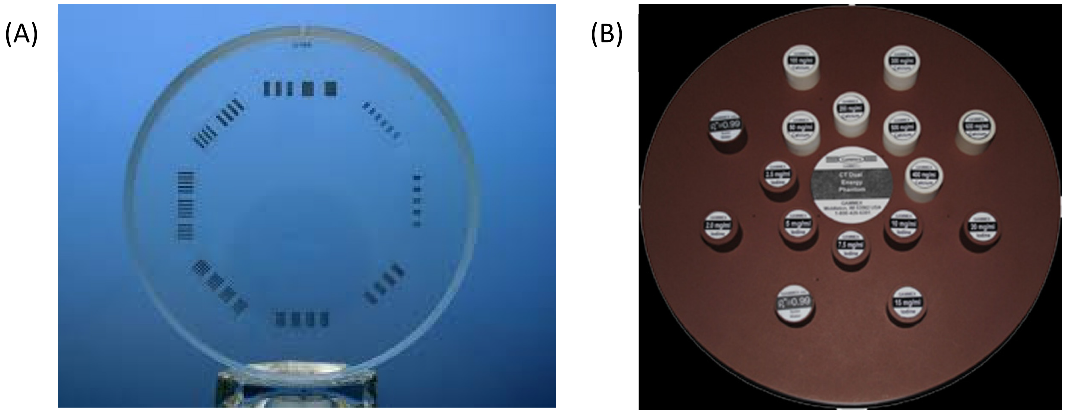

Figure 11: Different physical phantoms. (A) Line-pair phantom (JRT Associates, 2010) (B) Dual Energy Characterization CT Phantom made by homogeneous iodine solution with different concentrations (Gammex, 2014)

As mentioned in Section 1.4, we need anthropomorphic phantoms which have structures exhibiting controlled texture properties (beyond piecewise constant organ delineation) in CT images to help evaluate image quality under more sophisticated experimental settings and bring more clinical relevance to the study.

The development of anthropomorphic phantoms is boosted by the advancement in 3D printing technology. Based on previously acquired medical images, one may use state-of-art 3D printers to reproduce complex body tissues such blood vessels and different organ components. Rethy *et.al* developed a realistic-looking liver phantom as shown in the following [13]:

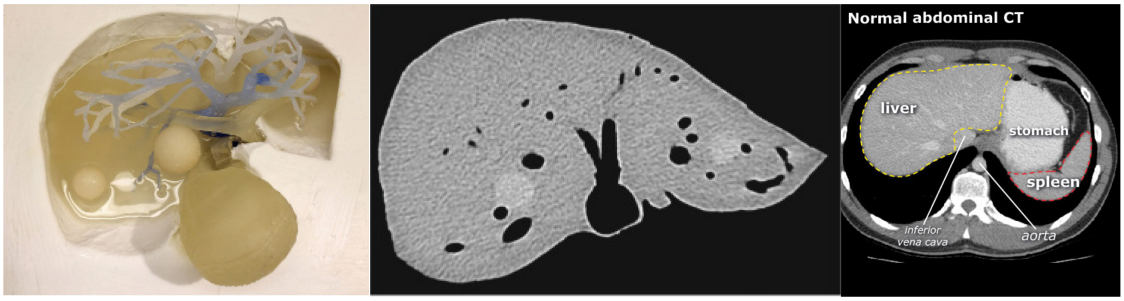

(A) (B) (C)

Figure 12: The application of a 3D-printed liver phantom. (A) The cross section of the liver phantom (B) The CT scan of the liver phantom (Rethy *et al*, 2017) (C) The clinical CT scan of the human abdomen (Dalrymple *et al*, 2009)

Although realistic and exhibiting high structural similarity to a real liver, this methodology has two potential limits: first, it requires an advanced 3D printer and specially designed material, which are both very expensive; second, since it's based on the previously acquired scans, it cannot be customized to generate random texture features, which limits the generality of the image quality assessment.

Facing these problems, we intend to come up with a generalized anthropomorphic phantom development strategy. We aim to design a digital phantom model which is capable of simulating a variety of texture features by customizing its parameters, and it should be able to be printed in the most commonly seen 3D printers for the purpose of fast-prototyping. Thus, a wide varieties of texture features may be generated to further investigate the impact of advanced reconstruction algorithm and different CT scanners on the detectability and radiomic quantification of different anatomical texture features. In the following sections we detail phantom development efforts using 3D-printing technique; note that the stenotic vascular phantom serves as a separate application to assess CT image quality.

2.2 Procedural Texture Phantom Development

We have developed a texture generation procedure based on constrained sphere packing within specific objects. Specifically, the spheres define voids within a specific control volume, e.g., a cylinder, cube, sphere, etc.; and these voids have customizable parameters which control their sizes, heterogeneity, and the degree of intersection. Such customization of the sphere sizes and degree of intersection permits a wide range of possible textures.

The workflow for procedural phantom generation is shown below:

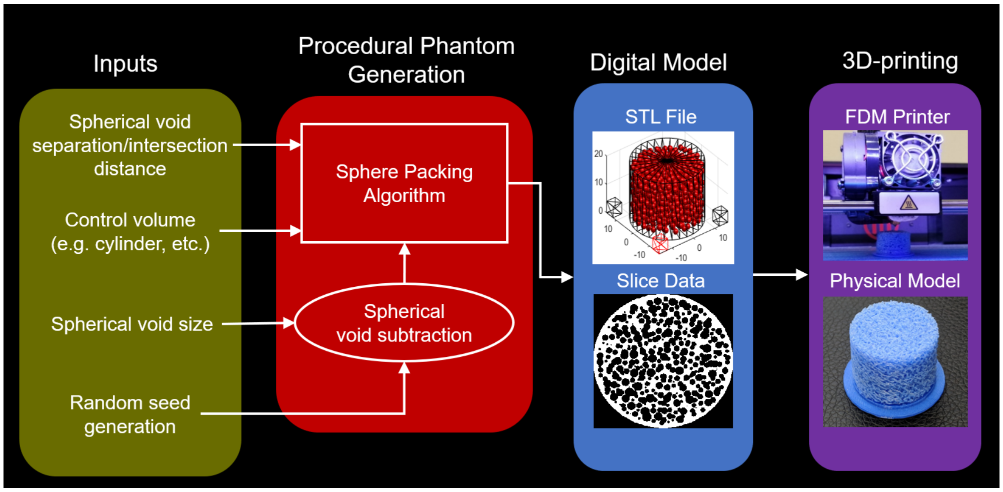

Figure 13: The workflow of the procedural anthropomorphic phantom development

First, we define the size of the control volume and generate spheres in the confined space. Our MATLAB implementation permits specification of geometrical parameters (radius, location of the center of the sphere), limits (number of voids, overlap, etc.) and randomization of all the spheres. Second, the MATLAB model is imported into the software OpenSCAD, wherein a Boolean difference operation is used to create voids (equivalently the spherical void subtraction) in predefined positions. Third, an STL file is generated based on the generated model. Finally, we use Simplify3D to convert the STL file into gCode and specify the parameters for the Fused Deposition Modeling (FDM) 3D printer.

The underlying logic of the proposed anthropomorphic phantom development lies in the microstructural similarity of our target textures: lung texture, trabecular bones and contrast-enhancing lesions (e.g. Hepatocellular Carcinoma (HCC) in liver), which may all modeled by porous structures. However, certain parameters need to be specified when generating different anatomical textures. For the lung texture, homogeneous voids with the same radius are generated inside a cylinder, while overlapping among voids are not allowed; for the trabecular bone texture, heterogeneous voids with radius in a certain range are generated, along with the degree of overlapping selected from a certain range. Finally, for the HCC liver lesion, either homogeneous voids with the same radius and a fixed degree of overlapping are generated in a large sphere, or they are evenly distributed surrounding a randomly shaped voids in the large sphere, such that the resulting phantoms are able to emulate different presentations of HCC liver lesions (e.g. different phases, state of disease, etc.).

2.3 Stenotic Vascular Phantom

A stenotic vascular phantom was designed with 15 hollow cylinders located radially throughout the cylindrical phantom body with 25mm diameter [14]. These hollow cylinders emulate vasculature with different diameters, as well as varying degrees of stenosis using constant near the ends of the large cylinder body, and narrowing the cylinder towards the center and reach the minimum diameter at the center layer of the cylinder body. Such design allows us to directly assess the spatial resolution and performance in angiography tasks across different CT systems by comparing the measured diameters in CT reconstructions to the ground truth. A summary of the range of diameters of these hollow cylinders is shown as follows:

Table 1: Design of the diameters of the stenotic vascular phantom

Maximum Diameter (mm)	Minimum Diameter (mm)				
4	0.3	1.225	2.150	3.075	4.000
3	0.3	1.200	2.100	3.000	/
2	0.300	1.150	2.000	/	/
1	0.300	1.000	/	/	/
0.5	0.300	/	/	/	/

Also, the perspective view of the phantom is shown as follows:

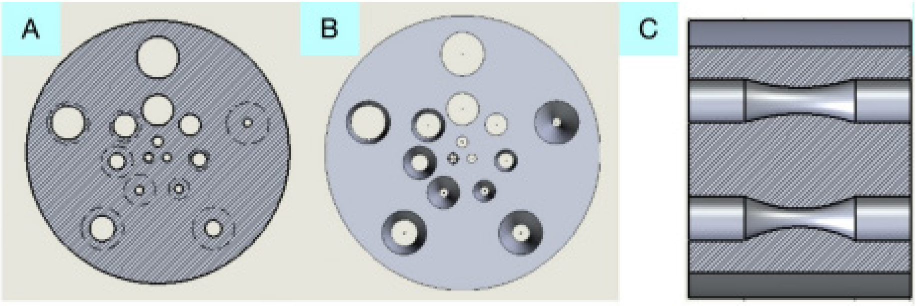

Figure: 14: The design of the stenotic vascular phantom. (A) and (B) Top view and (C) Sagittal view(Shi, 2019)

2.4 3D Printing Techniques: Fused Deposition Modeling (FDM) and Stereolithography (SLA)

FDM is a 3D printing process that uses a continuous filament of a thermoplastic material [15]. Typically, one FDM 3D printer is characterized by three key components: the filament being wound onto the spool, the extruder and the heating platform where the object is being printed upon. Photograph of the FDM printer used in this work is shown below:

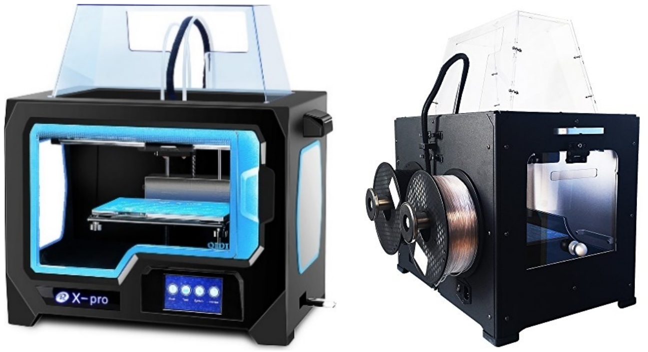

Figure 15: Front-view and back-view of the FDM 3D printer (Qidi Tech, 2020)

The printing process may be divided into three steps. First, the filament being wound on the spool is pulled into the cold end of the extruder, which comprises of two rollers on both sides, exerting roller-based torque to the material and controlling the feed rate by a stepper motor, and further be fed into the hot end of the extruder. Second, in the hot end, which comprises of the liquefier, heating chamber and the nozzle, the material is molten and transformed in a thin liquid, then exits from the nozzle and adheres to the previous material it is laid on. Third, the 3D printing process is performed in a layer-by-layer fashion by starting from the heating platform, with the extruder moved in the path defined by the desired printed shape. The extruder follows the planar path to deposit one layer; and moves horizontally by a small amount to begin a new layer. A schematic of the internal structure of the extruder is shown as follows:

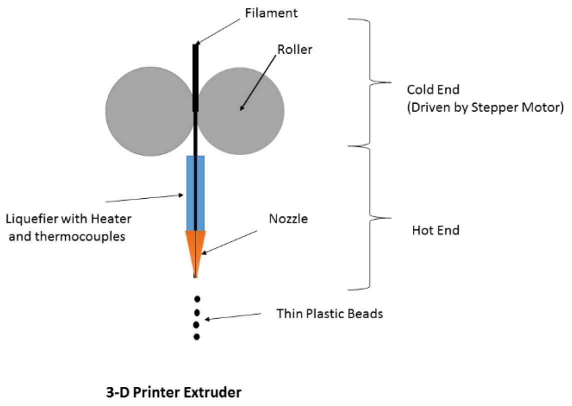

Figure 16: Detailed internal structure of the 3D printer extruder (Priybrat, 2014)

There exist numerous choices for 3D printers and filaments, such as Acrylonitrile Butadiene Styrene (ABS) and Polylactic acid (PLA) with trade-offs between strength and operating temperature, as well as the specific use. However, for all anthropomorphic phantom development, the following devices are used consistently: a QiDi Tech X-pro 3D printer and the Polylactic Acid (PLA) filament, whose attenuation coefficient is close to that of the human soft tissues.

Another commonly used 3D printing technology is Stereolithography (SLA). Such printers are used for creating models, prototypes, patterns and production parts, also in a layer-by-layer fashion, by using photochemical processes in which light causes chemical monomers and oligomers to cross-link together to form polymers [16]. In one common form, an SLA 3D printer focuses an ultraviolet (UV) laser onto the photopolymer resin, which is sensitive to the UV laser light and photochemically solidified, thus forming one layer of the desired shape predefined by the computer-aided-design (CAD) software. During the printing process, the photopolymer is contained in a vat and lowers its position per layer with respect to the building platform, and the above process is repeated until the object is printed. After the printing process, the object is typically washed using a 95% alcohol solution to remove the uncured resin.

For the stenotic vascular phantom development, we use the Moai Peopoly 3D printer shown below:

Figure 17: The Moai Peopoly SLA 3D printer (Peopoly, 2020)

There exist several trade-offs between FDM and SLA 3D printing technologies. First is the cost: typically an FDM 3D printer and the filament are cheaper than an SLA 3D printer and the resin. Second is flexibility of the material types: the FDM 3D printer can print objects with a variety of materials, ranging from PLA, ABS to metal-doped plastics. Multiple materials can even be printed using dual-extruder. In contrast, an SLA 3D printer can only print the objects with a single material and limited choices of resins. Third, printing resolution differs: specifically, the SLA printer can generally achieve much finer structures than the FDM 3D printer. In summary, the choice of different 3-D printing technologies depends on the budget and desired properties of the objects.

2.5 Contrast Control

Due to the limited materials available for printing, we require alternate strategies for varying contrast of targeted textures. Our solution is to immerse single material phantoms into fluids with different attenuation coefficients (such as potassium phosphate or iodine solution) to achieve various levels of contrasts and emulate different *in-vivo* targets. Such control allows us to further study the impact of CT acquisition protocol and reconstruction algorithm on the texture of target contrast, thus we have developed a strategy for controlling the attenuation coefficients of the fluids in which the phantom is being immersed.

The following method is proposed to precisely control the contrast level of the fluid. Through controlled experiments (X-ray source operated under 80 kVp and 40mAs), we find the expected linear relationship between the potassium phosphate concentration in the water and the Hounsfield Unit (HU) [17]. The mathematical relationship is shown as follows:

$$HU = 2.418 * c - 1.060 \qquad (12)$$

Where: c is the concentration of potassium phosphate in the water in mg/mL.

In this fashion we control the contrast in the anthropomorphic phantoms we have developed. For the trabecular bone phantoms, they were immersed in the solution with different potassium phosphate concentration; for HCC liver lesion phantoms, the contrast enhancement simulated HCC liver lesion in different phases; for the stenotic vascular phantoms, they were also processed in the same fashion to explore the influence of contrast level on the spatial resolution of different CT scanners.

2.6 Experimental Setups

The following section describes the experimental setups for each phantom experiment. For the study of phantom texture reproducibility and the assessment of CT system repeatability, a custom Cone-beam CT (CBCT) testbench was used, which comprised of a Varex Paxscan 4343CB detector and Varex Rad-94 X-ray source (Salt Lake City, UT). The pictorial illustration of the test bench is shown as follows:

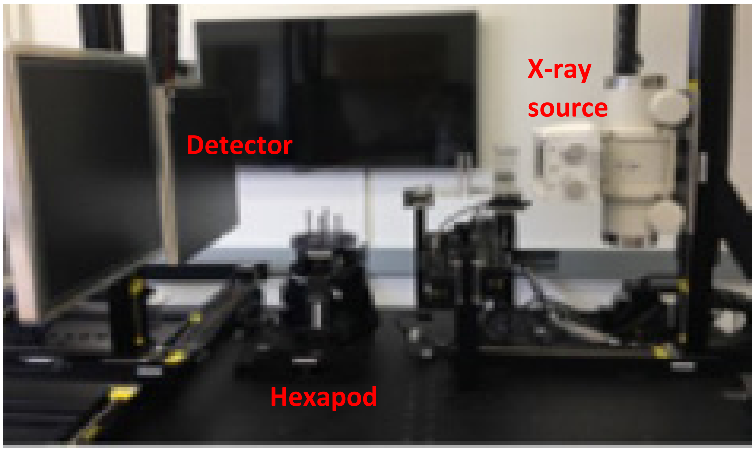

Figure 18: The CBCT test bench system

The geometrical parameters of this system are shown in Table 2:

Table 2: Geometry information of the CBCT test bench

Source and Detector Configuration	Source-detector Distance (SDD) (mm)	1113.82
	Source-axis Distance (SAD) (mm)	829.91

For CT system evaluation experiments, two other CT scanners were used. The first one was a Canon Aquilion Precision CT scanner (Otawara, Japan). The second one is a Bruker SkyScan 1172 microCT scanner (Billerica, MA).

2.6.1 Lung Texture Phantom Scans

The lung texture phantom was scanned both on the CBCT test bench 80 keV and 40 mAs total, as well as the micro-CT to generate a ground truth image. To assess performance on a clinical system, the texture insert was placed in a human body phantom and scanned by the Canon CT scanner by using the following eight imaging protocols:

Table 3: Different imaging protocols of the Canon CT scanner for the lung texture phantom

Protocol	1	2	3	4	5	6	7	8
Reconstruction Method	FBP	MBIR	FBP	MBIR	FBP	MBIR	FBP	MBIR
Tube Current (mA)	500	500	500	500	260	260	260	260
Exposure (ms)	500	500	500	500	500	500	500	500
Tube Voltage (kVp)	120	120	120	120	120	120	120	120
Convolutional Kernel	FC30	FC30	FC35	FC35	FC30	FC30	FC35	FC35
Focal Spot	0.6/1.3	0.6/1.3	0.6/1.3	0.6/1.3	0.4/0.5	0.4/0.5	0.4/0.5	0.4/0.5

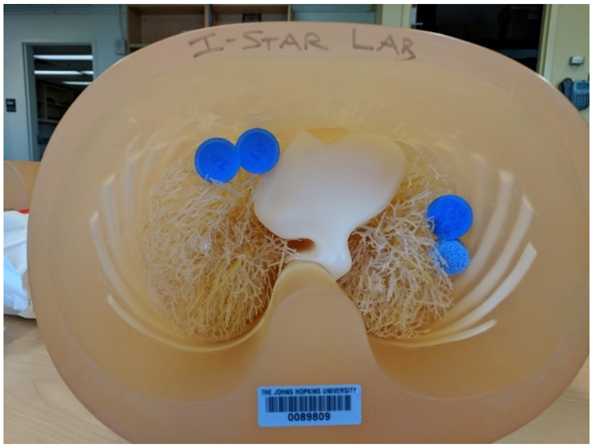

Figure 19: The lung texture phantoms being inserted into the human body phantom

Note that all the above imaging protocols operated in high-resolution mode. FBP and MBIR in the category of "Reconstruction Method" represent the Filtered Backprojection algorithm and Canon's implementation of a Model-based Iterative Reconstruction algorithm, respectively. The two types of Convolutional Kernel, FC30 and FC35, were used for normal-resolution or high-resolution reconstructions, respectively.

2.6.2 Trabecular Bone Phantom Scans

The main purpose of the image quality analysis for the trabecular bone phantoms was to evaluate the repeatability of the texture features. Ensembles of the trabecular phantom of the same design were printed in a repeated fashion. Phantoms were scanned by the CBCT testbench with the same settings as previously mentioned. All projection data were reconstructed by using FBP algorithm with Hamming windows with $a_0 = 0.55$ and apodization filter with 0.8 cutoff.

2.6.3 HCC Liver Lesion Phantom Scan

Different HCC liver lesion phantoms were immersed either in water or potassium phosphate solution to create different tissue contrast to simulate clinical observations of HCC liver lesion in different phases. Then they were scanned by CBCT test bench with the settings mentioned above.

2.6.4 Stenotic Vascular Phantom

Three identical stenotic vascular phantoms, which were immersed in iodine solution with concentrations of 10 mg/mL, 20 mg/mL and 50 mg/mL, respectively, were scanned by the CBCT testbench under insert-only setup and then inserted into the human abdomen phantom and scanned by the Canon CT scanner. The imaging protocols being used are shown as follows:

Table 4: Scanning settings of the Canon CT scanner for stenotic vascular phantoms

Protocol	Insert-only/Abdomen phantom	Tube Voltage (kVp)	Tube Current (mA)	Exposure (ms)	Convolution Kernel	Focal Spot	Reconstruction Method
CBCT test bench	Insert-only	80	40	30	N/A	N/A	FBP
Canon CT scanner, high resolution	Insert-only	120	100	500	FC15	0.4/0.5	FBP
Canon CT scanner, high resolution	Abdomen phantom	120	250	500	FC15	0.4/0.5	FBP
Canon CT scanner, normal resolution	Insert-only	120	100	500	FC11	0.4/0.5	FBP
Canon CT scanner, normal resolution	Abdomen phantom	120	250	500	FC11	0.4/0.5	FBP

2.7 Data Analysis, Results and Discussions

In the following sections, the data analysis, results and discussions grouped by each phantom are described.

2.7.1 Lung Texture Phantom

2.7.1.1 Data Analysis

All scans from the Canon CT scanner were registered with respect to the scan from CBCT test bench; and linear fitting was performed for intensity values to limit all scans within the same pixel intensity range for comparison. The same procedure was repeated for the scan from the micro-CT scanner for evaluation of the Canon CT scanner.

2.7.1.2 Results and Discussions

The Canon CT scans under the eight imaging protocols were registered and shown below:

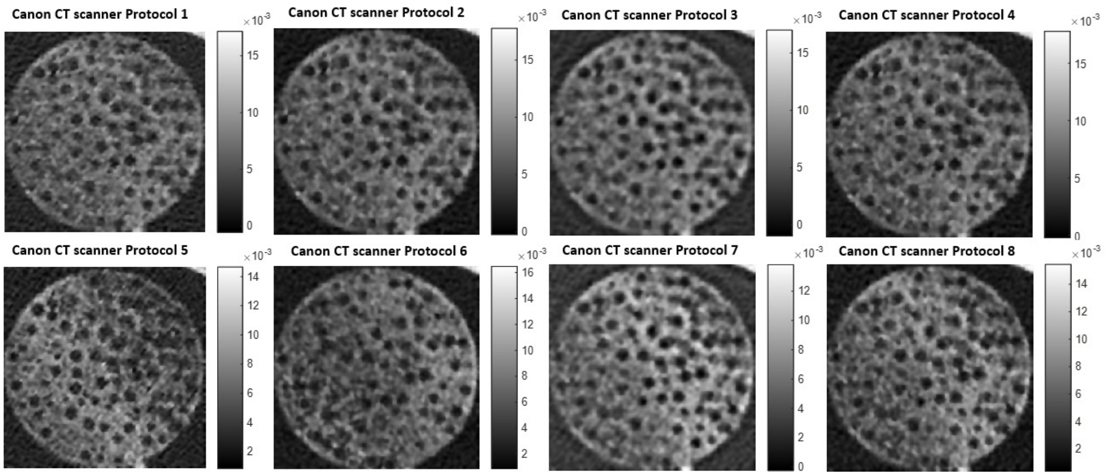

Figure 20: Canon CT scans of the lung texture phantom under eight different imaging protocols

Tube current, focal spot size, and reconstruction method all impact CT image quality. The reconstructions under higher tube current (500 mA, Protocol 1-4) showed lower noise level than the reconstructions under lower tube current (260 mA, Protocol 5-8). This is obvious when comparing the reconstruction Protocol 1 and 5, where the upper-right part of the latter is severely corrupted by noise, which results in heterogeneous tissue contrast over the phantom.

Focal spot size impacts the spatial resolution of the reconstructions. Reconstructions with larger focal spot size (Protocol 1-4) suffer from lower spatial resolution than those with smaller focal spot size (Protocol 5-8), because smaller focal spot will introduce less blurring.

Different reconstruction methods impact both the spatial resolution and the noise properties. By comparing reconstructions of Protocol 3 (reconstructed by FBP) and 4 (reconstructed by MBIR), the latter exhibits lower noise level but also lower spatial resolution. This illustrates the intrinsic trade-off between spatial resolution and noise level.

In addition, scans from CBCT test bench and micro-CT scanner are shown below to help us assess the performance of Canon CT scanner:

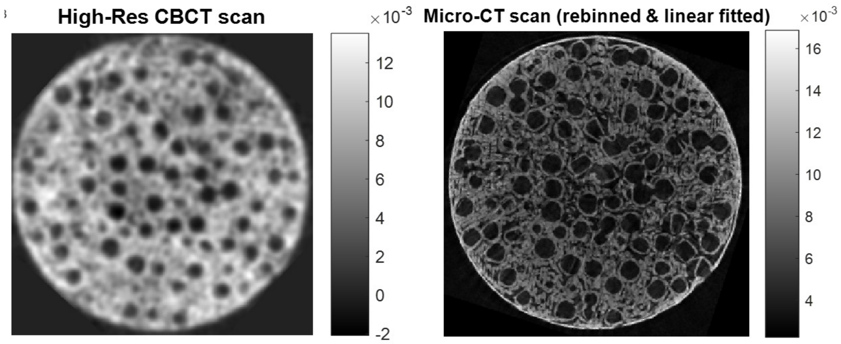

Figure 21: The CBCT scan and the micro-CT scan of the lung texture phantom

By comparing Figure 20 and 21, although corrupted by noise to different extents, scans reconstructed by using high-resolution kernel (FC35) from the high-resolution CT scanner from Canon succeeded in capturing texture features of the lung texture phantom and showed satisfactory qualitative agreement with scans from the other two CT scanners. This suggests the capability of high-resolution Canon CT scanner of capturing complex trabecular bone texture features in clinical use, which can help radiologists diagnose bone-related diseases more efficiently.

2.7.2 Trabecular Bone Phantom

2.7.2.1 Data Analysis

The analysis for the trabecular bone phantom was comprised of three parts. In the first part, we explored the impacts of the size of voids being generated inside the phantom on the repeatability of the texture features. Three sets of trabecular bone phantoms were generated with homogeneous voids inside with a random degree of overlap and whose diameters of the voids are 0.5, 1.0 and 2.0 mm. For each set of phantoms, three phantoms were printed to consider repeatability. After phantom printing, data collection and reconstruction, standard deviation maps across all three phantoms in each set were computed to assess the consistency of the texture features being reconstructed and the reliability of the printing quality.

In the second part, we explored the impact of the 3D printer nozzle size on the repeatability of trabecular bone texture features. We changed the 3D printer extruder nozzle from 0.4 mm diameter (used in the first part) to 0.2 mm diameter. Three sets of phantoms were generated in the same fashion as above. Standard deviation maps from the 0.2 mm diameter nozzle case were compared with those from the 0.4 mm diameter nozzle case to evaluate the textural difference. The summary of parameters of three sets of phantoms were as follows:

Table 5: Summary of parameters of trabecular bone phantoms for studying the impacts of void size and 3D printer nozzle diameter on texture feature repeatability

	Hole Diameter (mm)	Degree of overlapping (mm)	Number of voids	3D printer extruder nozzle size (mm)
Set 1	0.5	0 ~ 0.25	6000	0.4/0.2
Set 2	1.0	0 ~ 0.5	5673	0.4/0.2
Set 3	2.0	0 ~ 1.0	762	0.4/0.2

In the third part, we investigated the repeatability of more realistic and complex trabecular bone texture features. Trabecular bone phantoms insert with the following parameters were printed six times in a repeated fashion to generate variance maps for repeatability studies:

Table 6: The parameters of realistic trabecular bone phantom

Hole Diameter (mm)	Degree of overlapping (mm)	Number of voids	3D printer nozzle size (mm)
0.5 ~ 2.0	0.25 ~ 1.0	5500	0.4

In addition to standard deviation maps, the following geometric measurements of microarchitecture were chosen to aid the evaluation of the repeatability of the trabecular bone texture feature. They were trabecular thickness (Tb.Th), trabecular spacing (Tb.Sp) and bone-tissue volume fraction (BvTv). In basic bone research, Tb.Th and Tb.Sp are key measures characterizing the 3D structure of cancellous bone; while BvTv is an important indicator of osteoporosis and many bone-related diseases. To calculate these geometric measurements of bone microarchitecture, the following postprocessing steps are necessary: first, the trabecular bone need to be segmented apart from the tissue; second, morphological operations are performed to extract the thickness information. These steps are illustrated in the following figure:

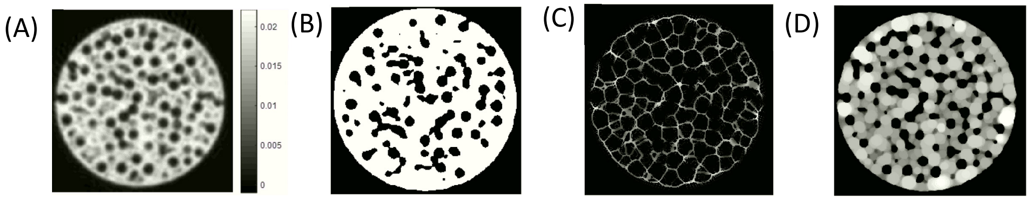

Figure 22: Postprocessing steps for calculation of geometric measurements of bone microarchitecture. (A) Original scan of the trabecular bone phantom (B) The segmentation of bone from tissue (C) The ridge information and (D) The thickness information extracted from the segmentation by using morphological operation

The geometrical interpretation of these measurements of bone microarchitecture may be visualized as follows:

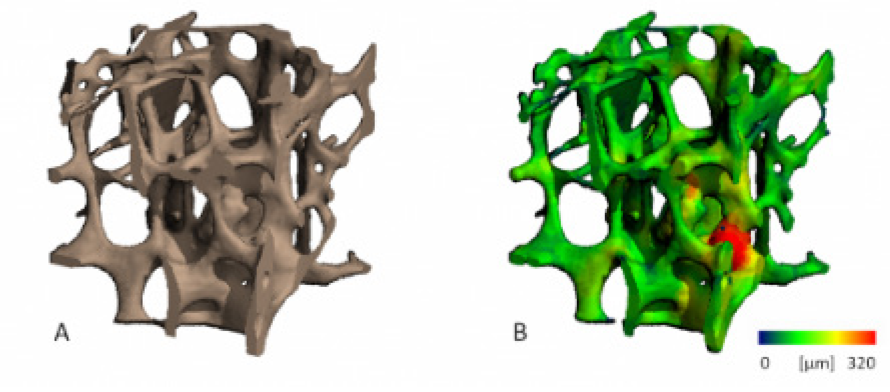

Figure 23: Geometrical interpretation of Tb.Th and Tb.Sp. (A) The 3D structure of the trabecular bone (B) Local thickness information of the trabecular bone (Martin, 2012)

Once the 3D structure of the trabecular bone is extracted from the bone segmentation, local thickness could be calculated everywhere, and the Tb.Th is the average of local thickness across the entire 3D structure. Tb.Sp is calculated in a similar fashion, except that the information of the inverse of the structure is used, which represents the average separation of the struts. The BvTv is self-explanatory and easy to compute.

2.7.2.2 Results and Discussions

The CBCT scans of three sets of trabecular bone phantoms printed by using the 0.4 and 0.2 mm nozzle were shown below, along with the standard deviation maps:

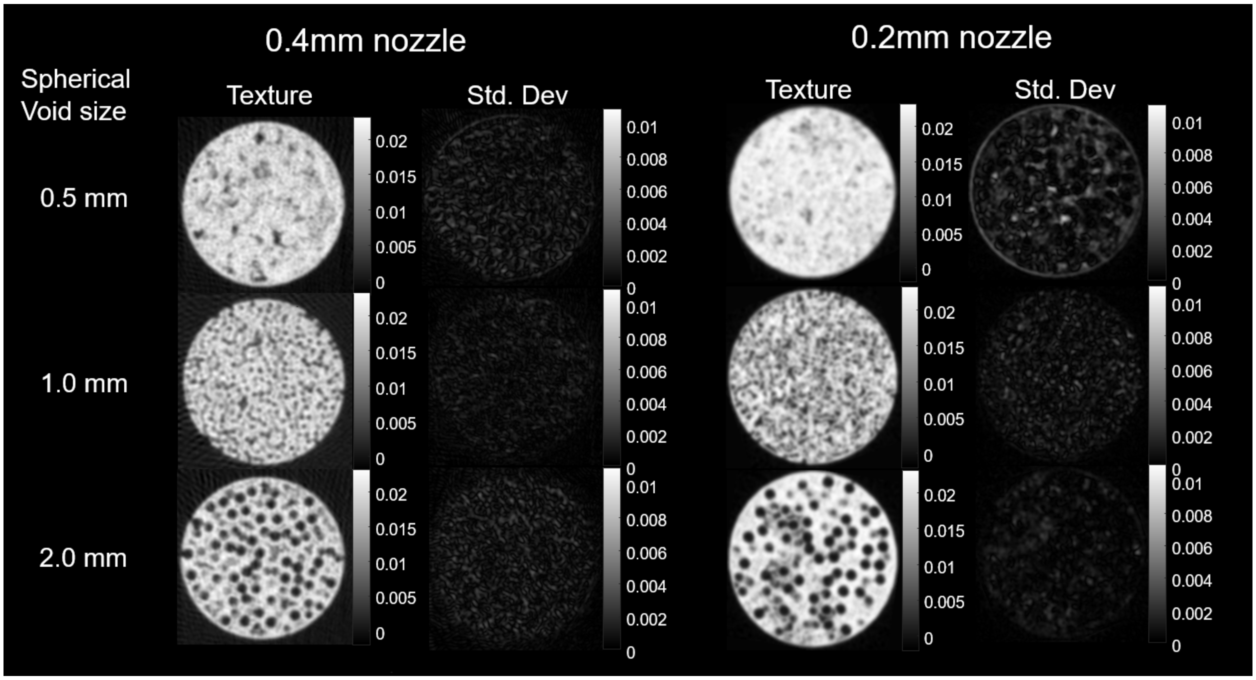

Figure 24: CBCT scans of trabecular bone phantoms printed by 0.4/0.2 mm diameter nozzles, along with the standard deviation maps

Both the trabecular bone phantoms printed by 0.4 mm and 0.2 mm nozzle exhibit high stability demonstrated by the relatively low standard deviations. However, the phantoms printed by 0.2 mm nozzle shows higher variability, which is mainly due to the unstable filament extrusion due to the smaller nozzle (e.g., the printer is more sensitive to nonuniformity of filament diameter, etc.). The 0.2 mm case had higher infill percentage and finer printing resolution, which is illustrated by more detailed texture features.

Notice that in both 0.5 mm spherical void size cases, there exist some voids which deviates from the designed homogeneous trabecular bone structure. This is mainly due to the limited printing resolution of the 3D printer, which failed to resolve fine texture features and skipped over an area of texture features which should have been printed. This problem is alleviated in 0.2 mm nozzle case with higher printing precision.

The trabecular bone radiomics calculated under each 3D printing settings are tabulated below:

Table 7: Trabecular bone radiomics calculated under the setting of 0.4 mm diameter nozzle

		Digital phantom (ground truth)	Cylinder 1	Cylinder 2	Cylinder 3	Mean	Standard deviation
Set 1	Tb.Th (mm)	2.266	3.257	3.091	3.156	3.168	0.084
	Tb.Sp (mm)	0.394	0.628	0.663	0.642	0.644	0.018
	BvTv	0.969	0.96	0.933	0.939	0.944	0.014
Set 2	Tb.Th (mm)	1.411	1.348	1.346	1.350	1.348	0.002
	Tb.Sp (mm)	0.891	0.694	0.679	0.704	0.692	0.013
	BvTv	0.781	0.748	0.755	0.805	0.769	0.031
Set 3	Tb.Th (mm)	2.285	1.906	1.868	1.881	1.885	0.019
	Tb.Sp (mm)	1.797	1.285	1.248	1.249	1.261	0.021
	BvTv	0.737	0.812	0.813	0.813	0.813	0.001

Table 8: Trabecular bone radiomics calculated under the setting of 0.2 mm diameter nozzle

		Digital phantom (ground truth)	Cylinder 1	Cylinder 2	Cylinder 3	Mean	Standard deviation
Set 1	Tb.Th (mm)	2.266	1.823	2.202	2.882	2.302	0.536
	Tb.Sp (mm)	0.394	0.5828	0.542	0.481	0.535	0.051
	BvTv	0.969	0.853	0.898	0.938	0.896	0.042
Set 2	Tb.Th (mm)	1.411	1.321	1.271	1.313	1.302	0.027
	Tb.Sp (mm)	0.891	0.607	0.608	0.577	0.597	0.018
	BvTv	0.781	0.793	0.786	0.805	0.795	0.010
Set 3	Tb.Th (mm)	2.285	2.137	2.204	2.134	2.158	0.039
	Tb.Sp (mm)	1.797	1.319	1.323	1.442	1.361	0.069
	BvTv	0.737	0.812	0.813	0.813	0.813	0.001

In the 0.4 mm nozzle case, when the spherical void size is 0.5 mm, both Tb.Th and Tb.Sp are systematically overestimated because of the limited printing precision, which resulted in larger interspace among the holes. The situation gets reversed when the spherical void size is 1.0 mm and 2.0 mm, which may be explained by limited printing resolution and relative low infill percentage. While for BvTv, the deviation from the true values mainly comes from the deviation from the digital design due to limited printing resolution.

In the 0.2 mm nozzle case, all radiomics get closer to the true values because of the higher printing precision. However, the standard deviation is higher, which reveals the intrinsic trade-off between printing precision and stability for the 0.2mm nozzle.

The analysis for the trabecular bone phantom with heterogeneous voids follows the same procedure. The CBCT scan and the standard deviation map are shown below:

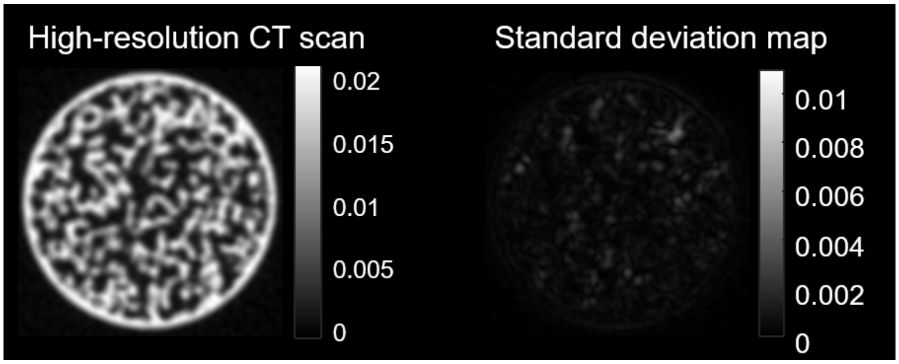

Figure 25: The CBCT scan and standard deviation map of the trabecular bone phantom with heterogeneous voids

And the radiomics calculated for all six printed phantoms are tabulated as follows:

Table 9: The radiomics of the trabecular bone phantom with heterogeneous voids

	Model Value ("True" value)	Cylinder 1	Cylinder 2	Cylinder 3	Cylinder 4	Cylinder 5	Cylinder 6	Mean	Standard deviation
Tb.Th (mm)	0.685	0.860	0.868	0.868	0.869	0.861	0.866	0.865	0.004
Error (%)	/	25.6	26.7	26.7	26.7	25.7	26.4	26.3	0.46
Tb.Sp (mm)	1.394	1.250	1.257	1.257	1.255	1.253	1.254	1.254	0.003
Error (%)	/	10.3	9.83	9.83	9.97	10.1	10.0	10.0	0.24
BvTv	0.427	0.403	0.400	0.402	0.401	0.404	0.402	0.402	0.001
Error (%)	/	5.62	6.32	5.85	6.09	5.39	5.85	5.85	0.25

From Figure 26 and Table 9, the CBCT text bench succeeded in consistently capturing more sophisticated texture features with relatively low standard deviations. Tb.Th is consistently overestimated while the Tb.Sp and BvTv are consistently underestimated. The error mainly comes from the deviation from the digital design due to limited printing precision.

In summary, we systematically investigated the impact of 3D printer nozzle size and spherical void size on the printing quality of the trabecular bone phantoms. We evaluated the ability of the CBCT test bench to reliably reproduce the texture features. Further studies have been conducted by Shi *et al* [18], where the printing precision has been improved by using SLA 3D printer, and different contrasts have been achieved by immersing trabecular bone phantoms into potassium phosphate solution with different concentrations. In addition, these trabecular bone phantoms were inserted into human body phantom and GLCM features were used to perform system evaluation across different CT scanners.

2.7.3 HCC Liver Lesion Phantom

The study of HCC liver lesion phantom aims to show the capability of the phantom simulating clinical cases. These phantoms were immersed in either water or potassium phosphate solution to achieve different tissue contrast, and their CT scans were compared with the clinical cases to evaluate their similarity.

The following four types of HCC liver lesion phantoms were printed:

Table 10: Description of four types of HCC liver lesion being printed

Type 1	An eccentric void with random shape + uniformly distributed small voids
Type 2	Heterogeneous void distribution: clustered large voids + uniformly distributed small voids
Type 3	Homogeneous void distribution: uniformly distributed small voids throughout the whole sphere
Type 4	A large spherical void in the center + small spreading voids (with diameter inversely proportional to the distance from the center of the large void)

The following shows the CBCT scans of Type 1&2 HCC liver lesion phantoms, which were placed in air, water or potassium phosphate solution:

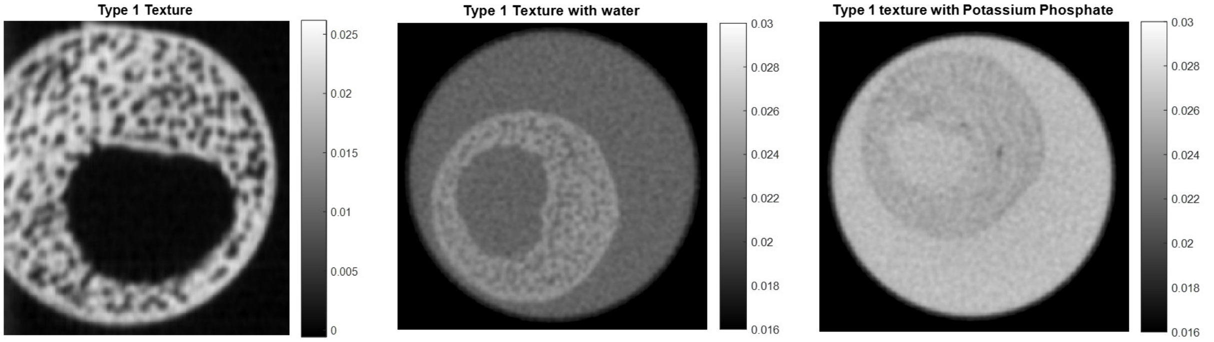

Figure 26: Type 1 textured phantom in air, water and potassium phosphate solution

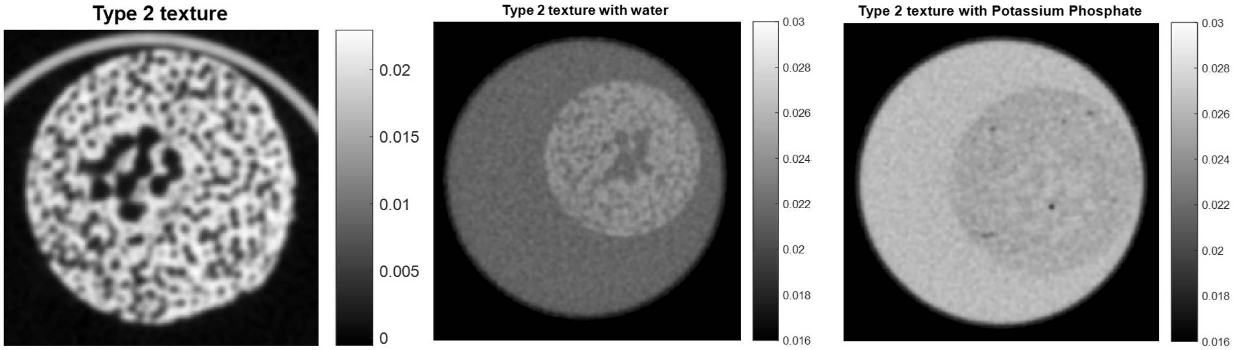

Figure 27: Type 2 textured phantom in air, water and potassium phosphate solution

Both Type 1&2 textured phantoms were used to simulate arterial phase CT image of the HCC liver lesion, which shows a hyperattenuating nodular lesion as follows:

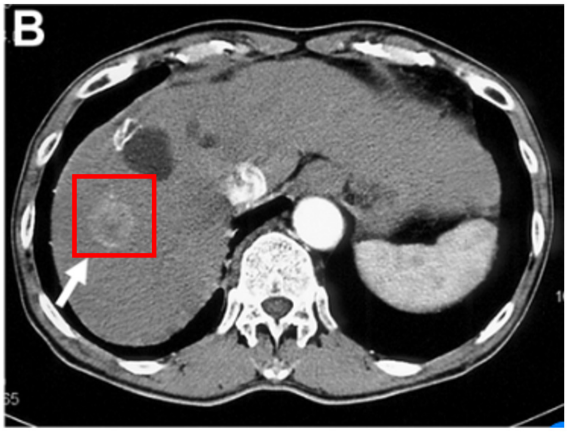

Figure 28: Arterial phase CT image of the HCC liver lesion (Masakatsu Tsurusaki, July 2014)

The CBCT scans of Type 3 texture features in air, water or potassium phosphate solution are shown below:

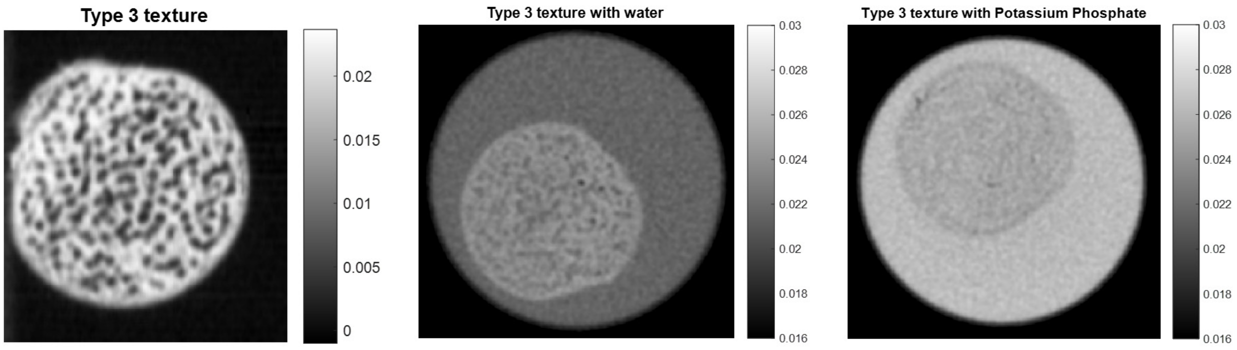

Figure 29: Type 3 textured phantom in air, water and potassium phosphate solution

The Type 3 textured phantom was designed to simulate portal phase and equilibrium phase of the HCC liver lesion by adjusting tissue contrast, which are both depicted as a discrete hypoattenuating nodule as follows:

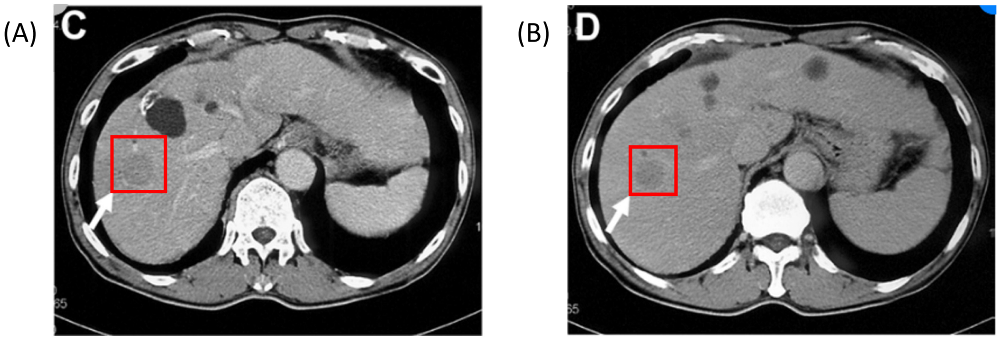

Figure 30: HCC liver lesions in different phases. (A) Portal phase (B) Equilibrium phase Both of them are depicted as discrete hypoattenuating nodules (Masakatsu Tsurusaki, July 2014)

Finally, Type 4 textured phantom was designed to generate some interesting texture features in HCC liver lesion, and the CBCT scans are shown in the following figure:

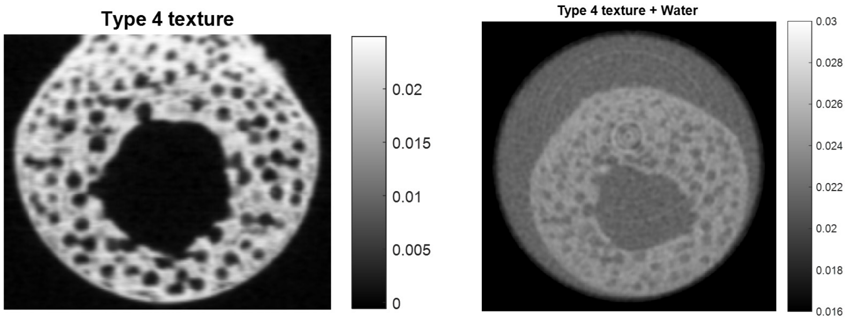

Figure 31: Type 4 textured phantom in air and water

In summary, all four types of HCC liver lesion phantoms illustrate the potential of contrast-enhanced phantoms with heterogeneous texture features simulating clinical cases. In the future, we plan to achieve different tissue contrast and insert these phantoms into the human liver phantom for clinical evaluation, which would bring about greater flexibility for emulating CT contrast-enhanced studies.

2.7.4 Stenotic Vascular Phantom

The purpose of this experiment is to evaluate the reliability of the Canon CT scanner in angiography applications.

2.7.4.1 Data Analysis

After data collection and reconstruction, the following postprocessing steps were used to calculate the diameter of each vascular region: first, we used k-means segmentation technique and applied the threshold on area to separate the cross-sections of vessels apart from the rest of the scan, which is shown below:

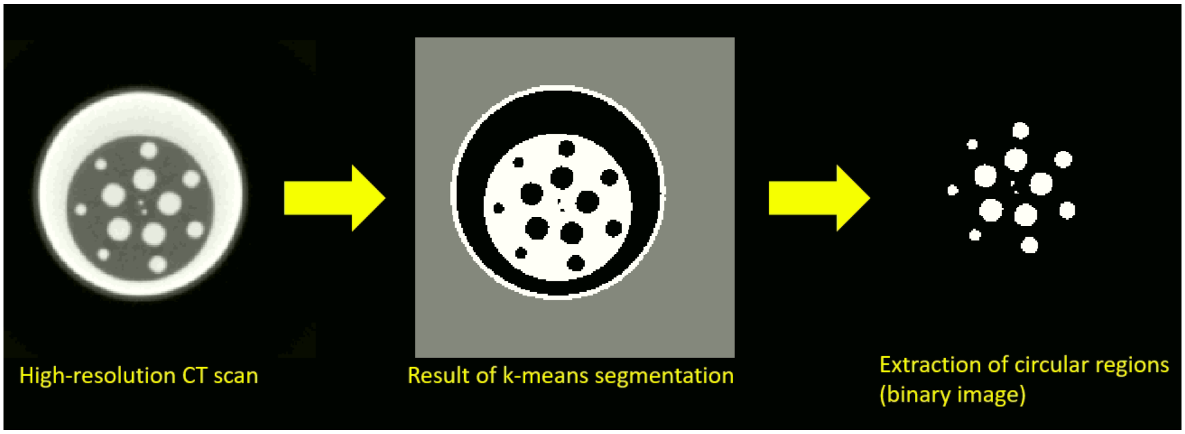

Figure 32: The workflow of extracting the vascular regions

Second, the MATLAB built-in function “regionprops” was used to fit in the circles which best match the extracted vascular regions, which is shown in the following figure:

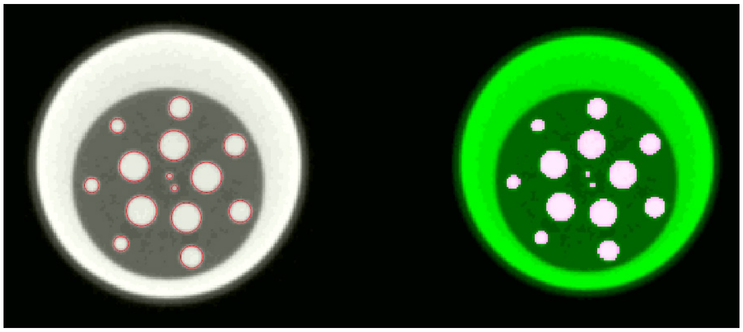

Figure 33: The fitted vascular regions overlaid on the original scans

These processes were performed repeatedly on all scans. Finally, plots showing how the radii of these vessel regions vary across different slices of the phantoms were used to evaluate the spatial resolution property of the Canon CT scanner.

2.7.4.2 Results & Discussion

The CT scans of stenotic vascular phantoms under different experimental settings were linear-fitted in HU to the Canon CT scanner case and registered, as shown below:

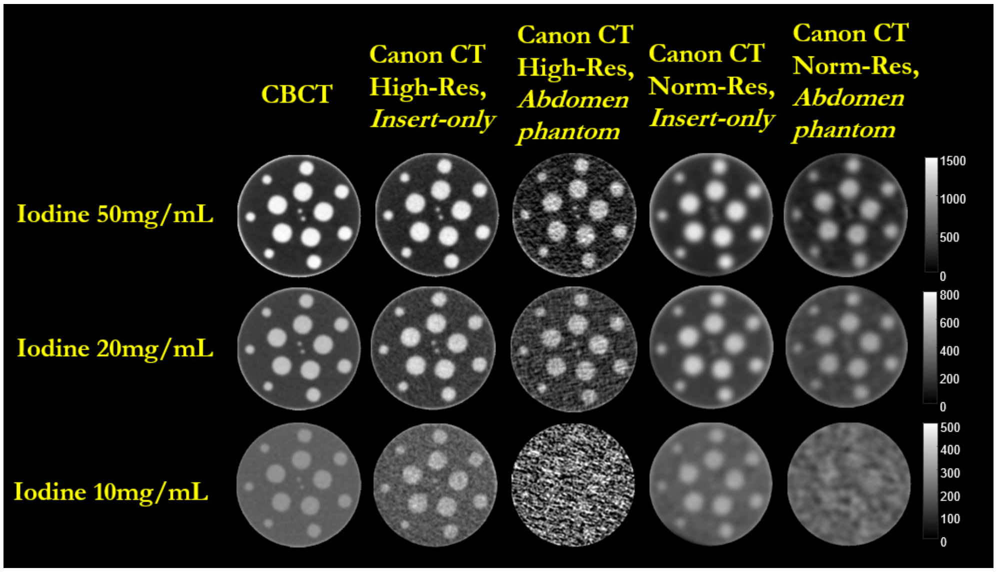

Figure 34: CT scans of stenotic vascular phantom under different experimental settings

Note that not all vascular regions are used to assess the performance of different CT scanners.

Vascular regions were indexed in the following figure:

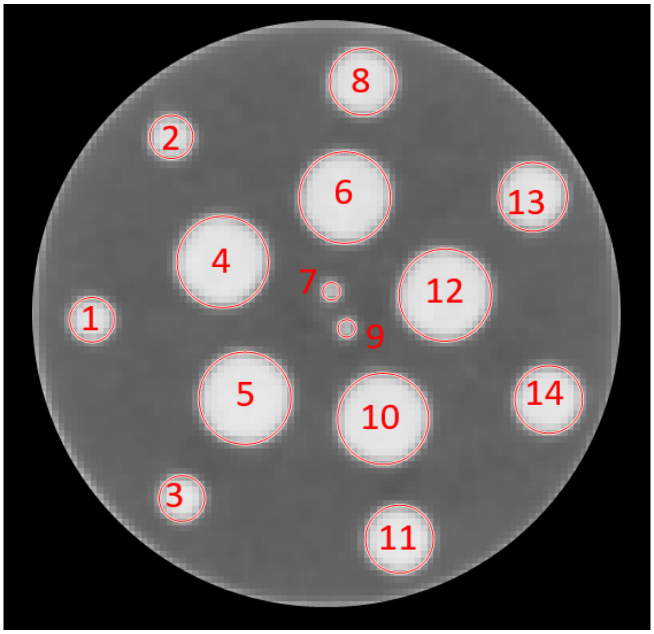

Figure 35: Indexing of all vessel regions

Among them, only vascular regions 1,3,4,5,10,11,12,13,14 were used for the assessment of spatial resolution property of the Canon CT scanner.

In addition, during the following discussion, the vessel radii calculated from the CBCT test bench serve as “ground truth” values for assessment of Canon CT scanner.

The following figure shows the vessel radius as a function of slice using iodine solution with a concentration of 10 mg/mL for the various locations:

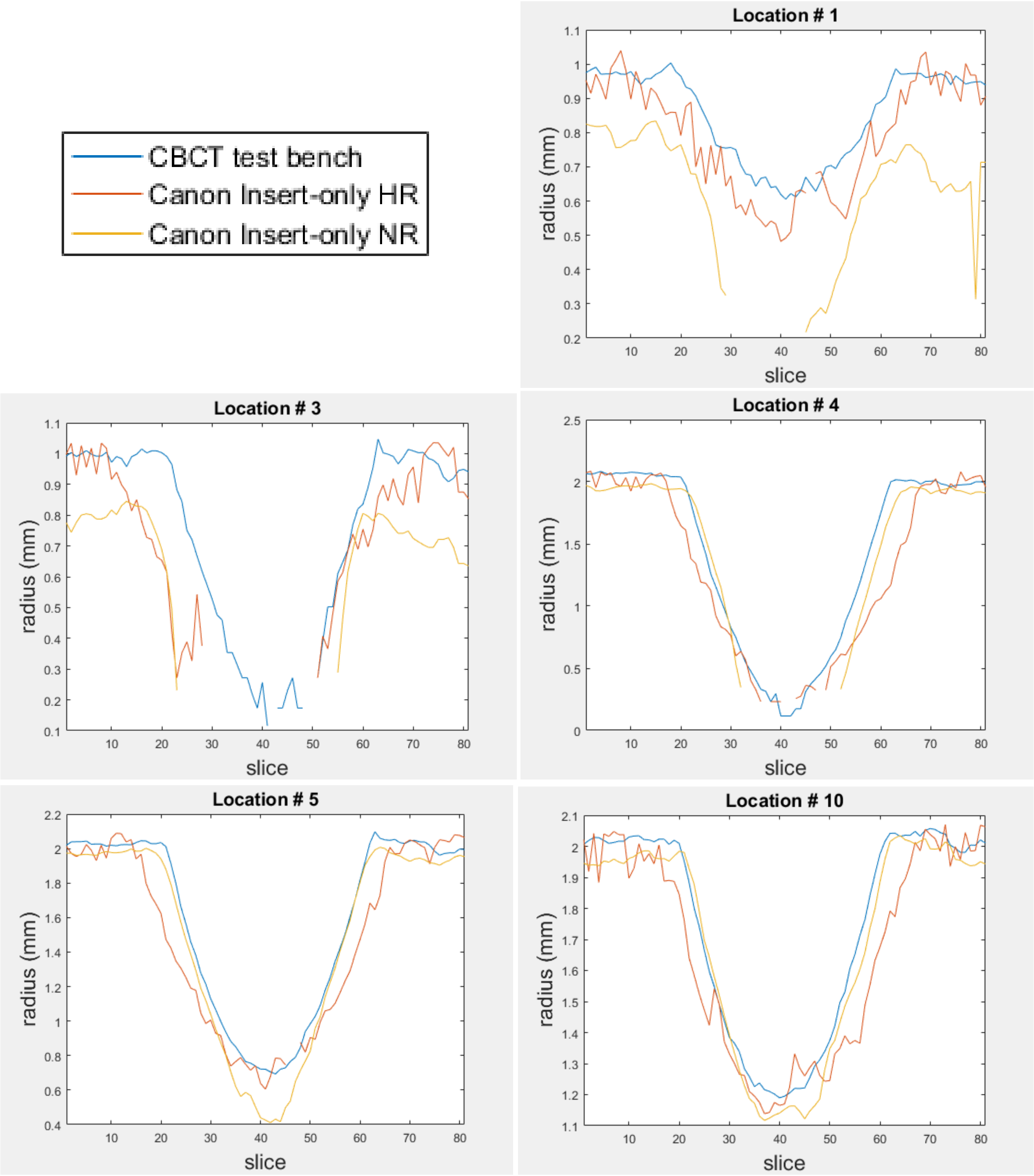

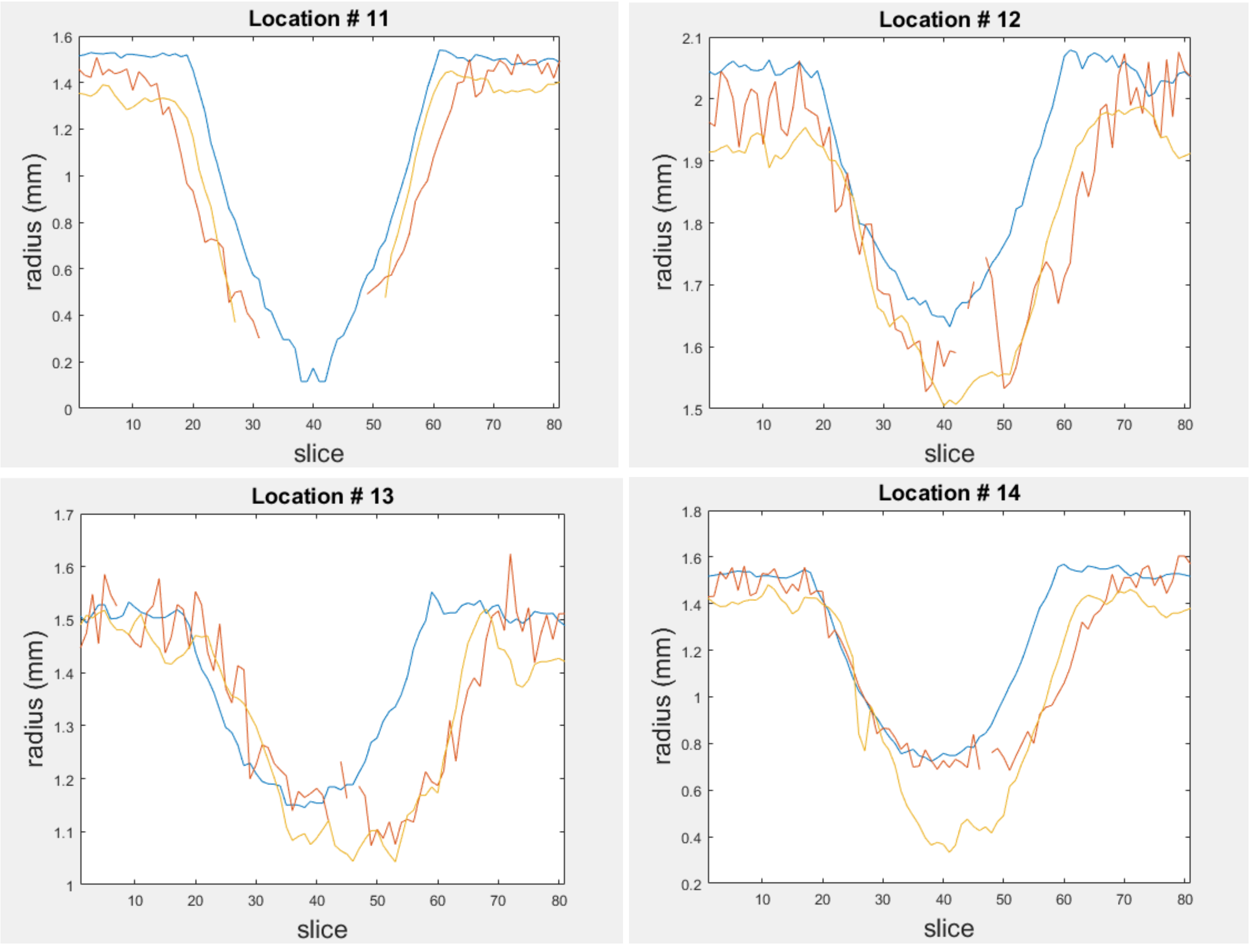

Figure 36: Comparison of vessel radius at different locations in iodine 10 mg/mL case

The radii from reconstructions with insert-only, high-resolution (HR) kernel are generally closer to CBCT "ground truth" results than the radii from reconstructions with insert-only, normal-resolution (NR) kernel, because the HR reconstruction helps preserve more details. On the other hand, the difference between radii from the Canon CT scanner and the CBCT "ground truth" is large because of the low vessel contrast, which results in inaccurate image segmentation during the postprocessing steps.

In addition, there are two interesting observations in Figure 36. First, there exist some discontinuities in the radius curve, which can be explained by the segmentation error during the postprocessing steps, which is illustrated with a failed detection:

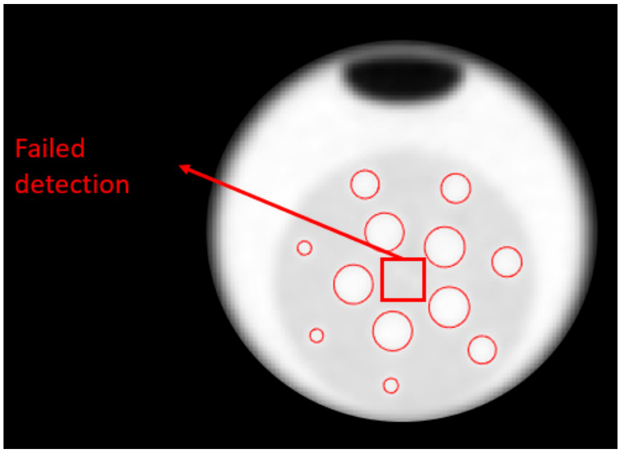

Figure 37: Pictorial illustration of a failed detection of vessel region

As the size of the vessel decreases near the central slice, the local vessel contrast also decreases. Both the smaller feature and lower contrast made it difficult for the vessel region to be segmented, thus leaving discontinuities in those radius curves.

The other observation is that we were unable to reliably find vessels in the following two imaging protocols:

Protocol	Iodine Concentration (mg/mL)	*Insert-only/Abdomen phantom*	Convolution Kernel
Canon CT scanner, Low resolution	10	*Abdomen phantom*	FC11
Canon CT scanner, High resolution	10	*Abdomen phantom*	FC15

Both cases used the inserts placed in the human abdomen phantom. The extra attenuation of the body introduces high noise levels. In combination with the low vessel contrast, the image quality is severely deteriorated as shown below:

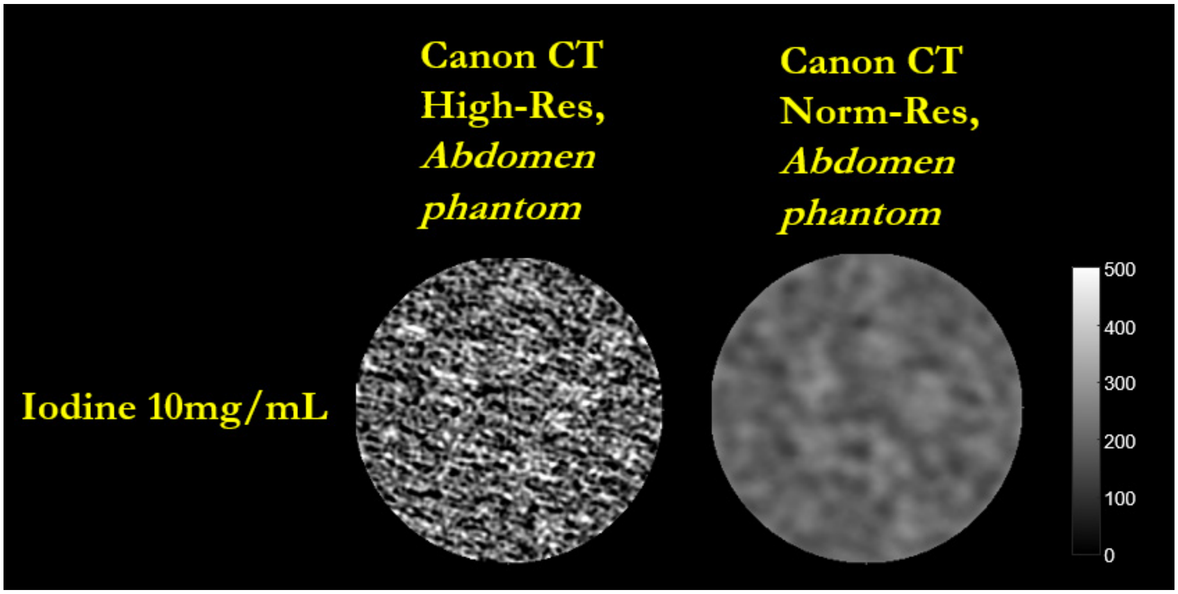

Figure 38: CT scans from the in-human abdomen phantom studies

In these cases, the vascular radius information failed to be extracted.

The following figure shows the vessel radius as a function of slice in iodine solution with a concentration of 20 mg/mL:

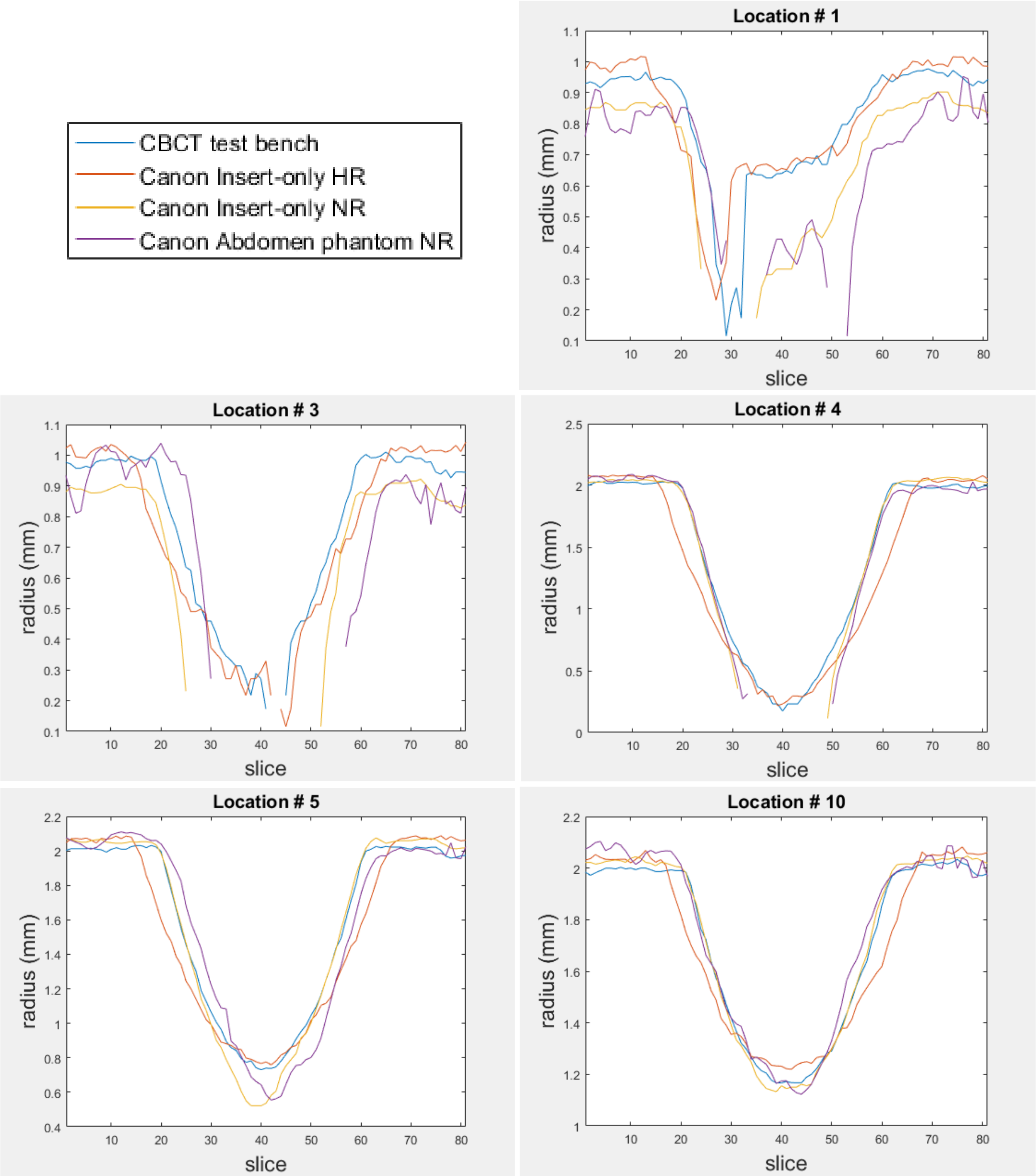

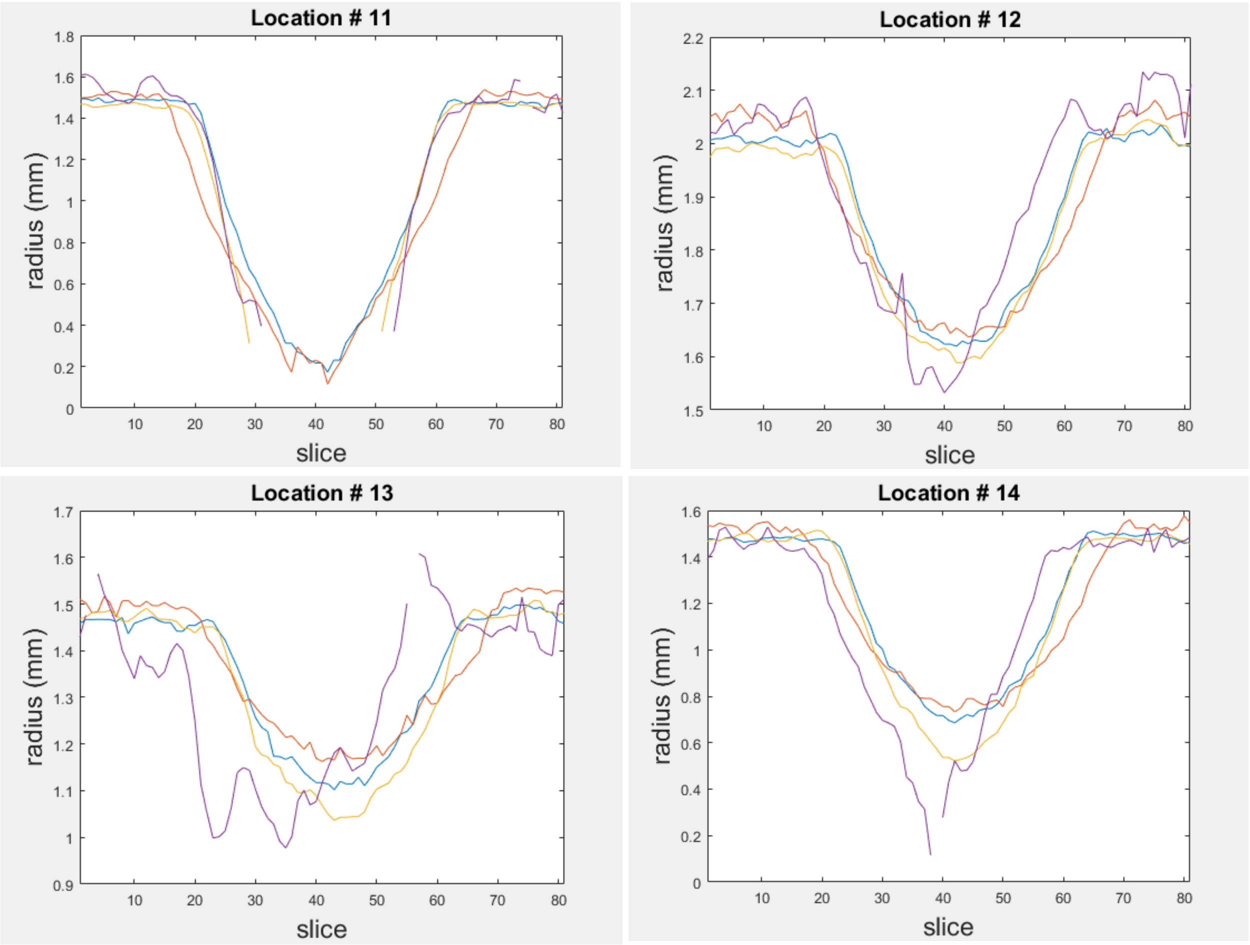

Figure 39: Comparison of vessel radius at different locations in iodine 20 mg/mL case

In this case, the radii from reconstructions with *insert-only,* HR kernel match the CBCT “ground truth” results well; while the radii from reconstructions with *insert-only,* NR kernel have greater error and larger deviations from the CBCT “ground truth” results. For radii from reconstructions of the insert in the abdomen phantom with NR kernel, even larger errors and more discontinuities are present, as compared with the other two imaging protocols. Note that the radii from the reconstructions of the insert in the *abdomen* phantom with HR kernel are missing because of slice-dependent noise, as shown in the following figure:

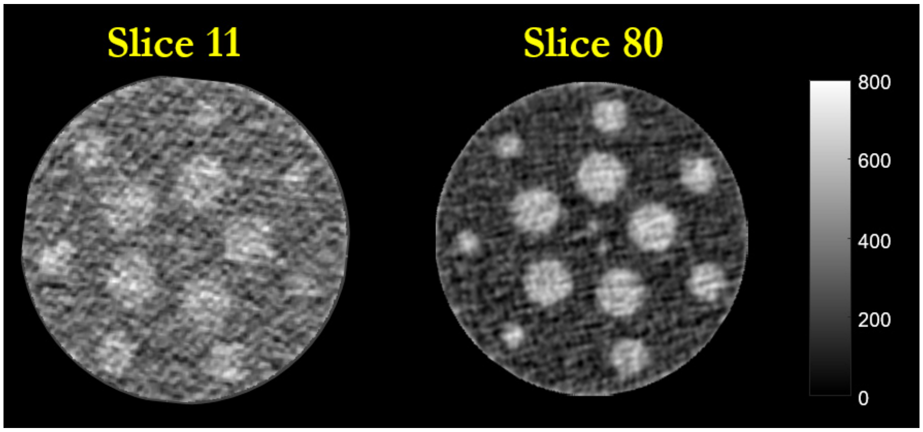

Figure 40: Slice-dependent noise deteriorates the detectability of vascular regions

Only the radii of certain vessel regions in few slices (less than 10) can be calculated, and the procedure of vessel region segmentation completely failed in all other slices. Thus those extremely scattered results are excluded from the report.

The following figure shows the vessel radius as a function of slice in iodine solution with a concentration of 50 mg/mL:

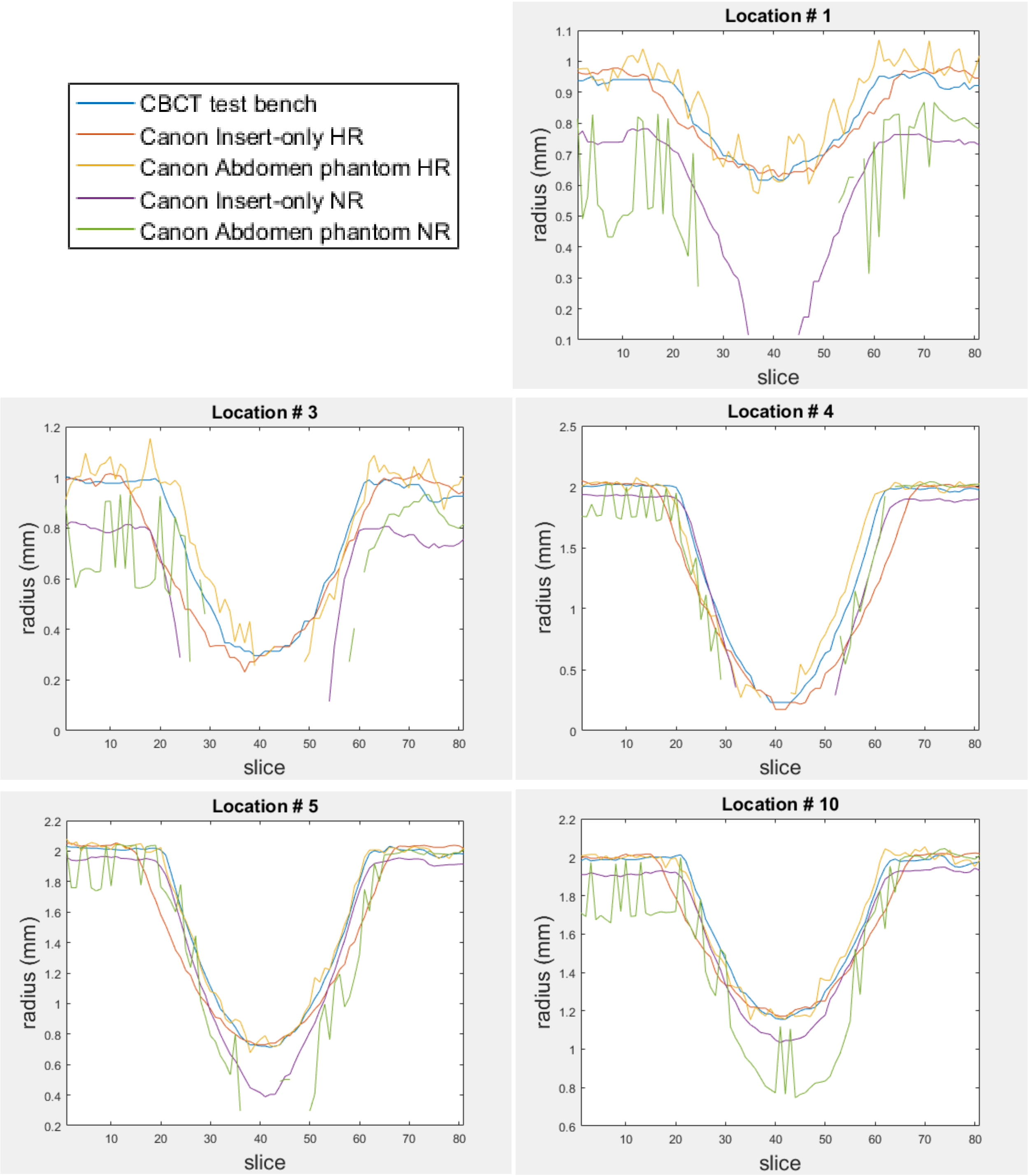

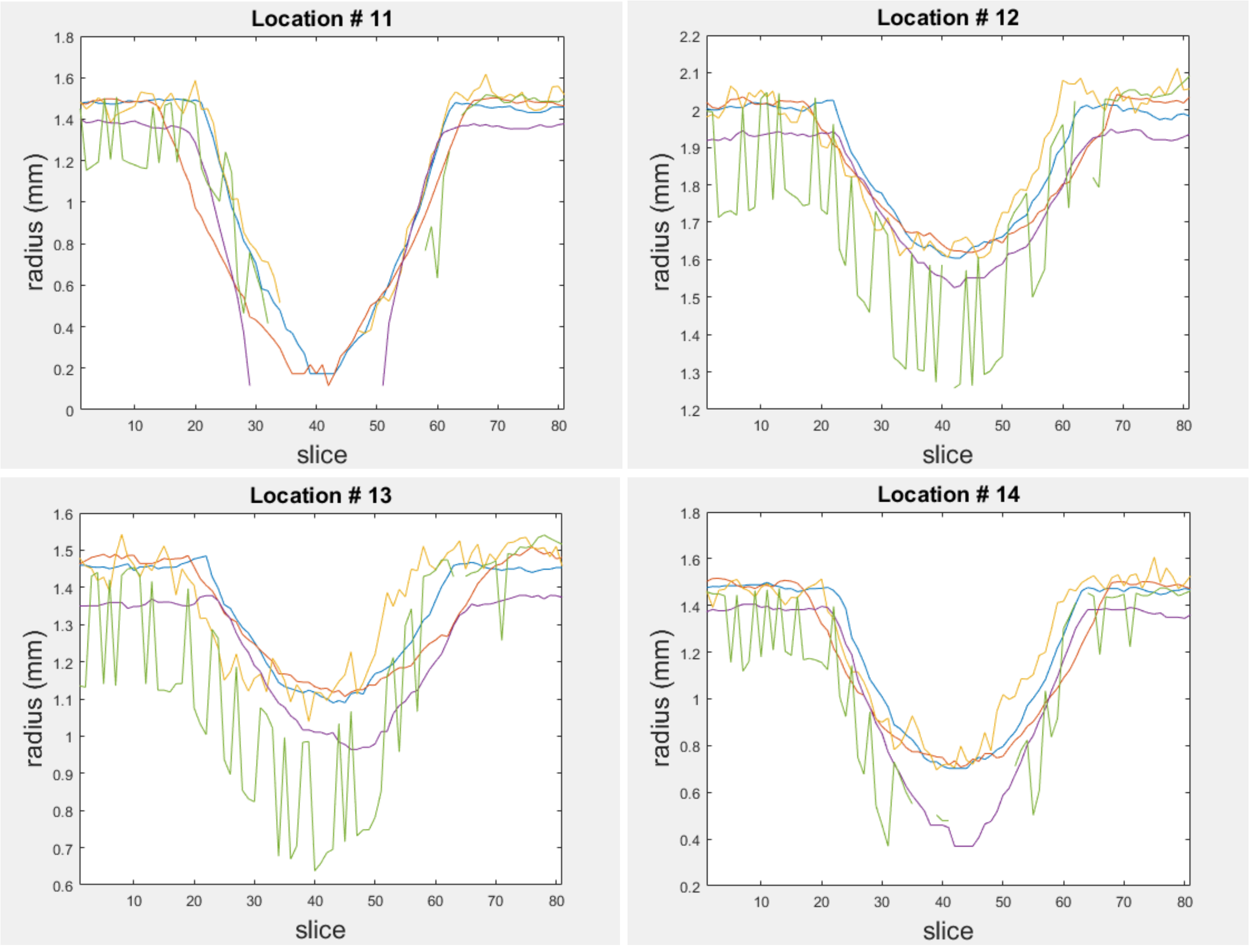

Figure 41: Comparison of vessel radius at different locations in iodine 50 mg/mL case

Radii from reconstructions under all imaging protocols are present due to the high vessel contrast. The radii from reconstructions with HR kernel better match the CBCT “ground truth” results and have almost no discontinuities; but for the radii from reconstructions with NR kernel, the deviations from the CBCT “ground truth” results are much larger. The radii from reconstructions of *insert-only* with NR kernel exhibit large fluctuations and many discontinuities, which shows the difficulty in resolving vessels in this case due to the high noise level.

In summary, the HR mode of Canon CT scanner generally does better job than the NR mode. However, low vessel contrast and the noise introduced by inserting the stenotic vascular inserts into the human abdomen phantom can make the extraction of vascular regions impossible for some contrast levels. The measurements of vascular radius exhibit location-dependent behavior: the radius curves at location 4, 5, 10 and 11 better match the CBCT “ground truth” results and generally have smaller fluctuation and fewer discontinuities than in other locations. A possible explanation is that when the stenotic vascular phantom was washed using a 95% alcohol solution, the uncured resin in vessel 4, 5, 10, and 11 were cleaned more thoroughly, thus resulting in more stable vessel contrast and vessel region segmentation. Lastly, the vessel size limit is defined as the smallest vessel radius reliably resolved (with no discontinuities within 5 slices) by the CT scanner. The pictorial illustration of vessel size limits is shown in the following figure:

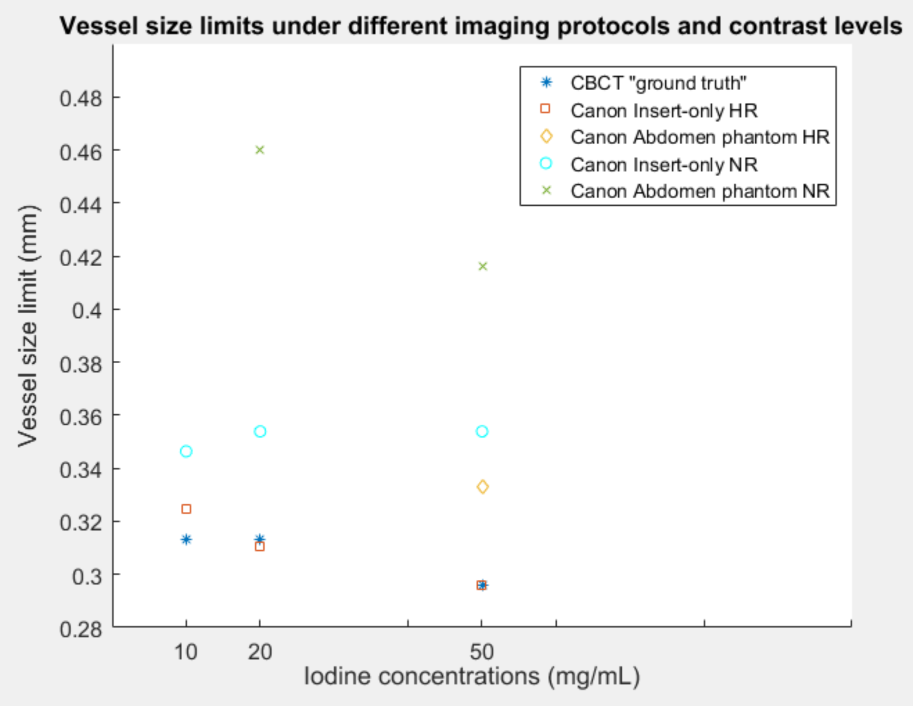

Figure 42: Vessel size limits under different imaging protocols and contrast levels

The vessel size limit is impacted by both vessel contrast level and different imaging protocols. Under the same imaging protocol, the vessel size limit decreases with the increasing vessel contrast level. Overall, the vessel size limit is sorted in ascending order as follows based on different imaging protocols: CBCT “ground truth”, Canon CT high-resolution with insert only, Canon CT high-resolution with insert in human abdomen phantom, Canon CT normal-resolution with insert only, Canon CT normal-resolution with insert in human abdomen phantom.

CHAPTER 3

3. Dynamic Fluence Field Modulation (FFM)

3.1 Background & Motivation

To achieve better dose distribution and dose reduction in X-ray Computed Tomography (CT), various techniques have been developed. Among these techniques, Fluence Field Modulation (FFM) has been routinely practiced. However, FFM with a static bowtie filter, which is adopted on commercial CT systems, has one main drawback: a single FFM pattern throughout the scan cannot accommodate the heterogeneity within the patient, oblateness of the patient cross-section and variations of patient size along the longitudinal direction [19]. To address these limitations, dynamic FFM has been proposed in which the X-ray beam shape may be a function of both the transverse detector direction and the projection angles [20]. In this work, we implemented dynamic FFM throughout the scan by using the previously designed Multiple Aperture Devices (MADs), which were fabricated using a tungsten laser sintering process and integrated into an X-ray CT bench [21].

For dynamic FFM, there is an important question: What kind of fluence field pattern should be delivered to the patient? Previous work for FFM optimization primarily focused on optimizing an objective based on image noise in Filtered Backprojection (FBP). One optimized solution gives the analytical form of FFM pattern that yields minimum mean variance within the reconstructed image [22]. However, this analysis is incomplete. First, image noise alone is insufficient as an image quality metric. The medical imaging community continues to move towards task-based performance assessments that consider both noise and resolution needed for specific diagnostic goals [23]. Second, model-based iterative reconstruction (MBIR) with its improved (and distinct) noise and resolution properties as compared with FBP is increasingly adopted on commercial CT scanners. These factors suggest that optimal FFM for FBP may not be optimal for MBIR. To tackle these two challenges, a task-driven imaging framework to optimize FFM for MBIR using a global task-based image quality objective has been developed [24].

In this work, we aim to validate the improvement of dynamic FFM, including optimizations based on task-driven metrics, over conventional FFM with static bowtie filter. To go beyond the traditional image quality metrics for evaluating different FFM imaging protocols, such as noise power spectrum (NPS) and contrast-to-noise ratio (CNR), a human observer study is designed.

3.2 Materials & Methods

3.2.1 Imaging Bench

Experiments were conducted on a cone-beam CT test bench with dual-MAD filters installed (Figure 43), which were manufactured from 2-mm thick tungsten plates with a pitch size of 0.9mm. Each MAD filter was attached to a linear actuator (Velmex Inc.,Bloomfield, NY) with translation encoding precision of 2 μm. The vertical centers of the MADs were aligned with the central vertical axis of the flat-panel detector to emulate the degree of beam divergence on a diagnostic CT scanner. The actuators can be controlled synchronously with the motion stage and a step-and-shoot x-ray exposure.

The benchtop system employs an x-ray source (CPI, Georgetown, ON, Canada) that has been customized to deliver view-dependent pulse width ranging from 0.1 to 60 ms, thereby enabling exposure modulation through pulse width control at a fixed tube current.

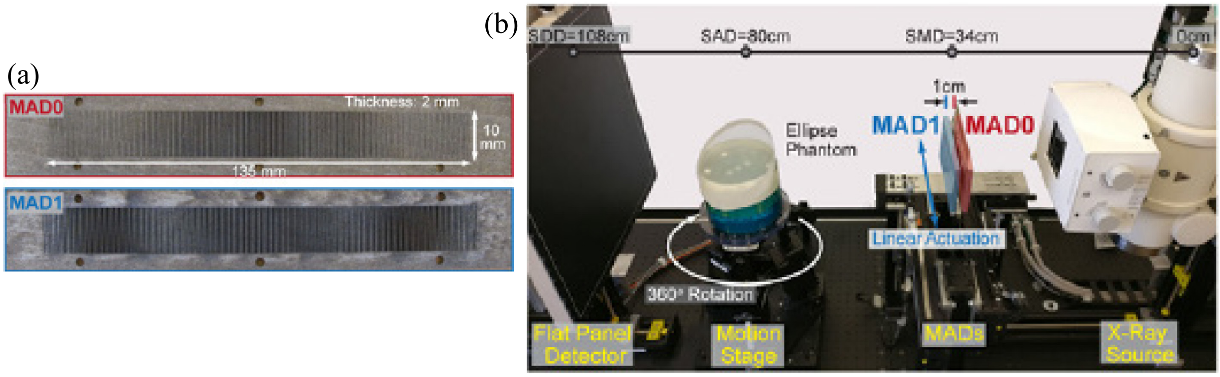

Figure 43: Experimental setups for dynamic FFM studies. (a) Dual MAD filters; (b) Experimental imaging bench with Dual MADs filters installed (Gang, 2019)

3.2.2 Imaging phantoms and phantom-specific FFM design

Two elliptical PMMA phantoms (major axis = 25.8 cm, minor axis = 14.1 cm) were employed. The first had 11 cylindrical vacancies, where the designed locations for stimuli inserts were indexed from one to five and highlighted (Figure 44a). Three different kinds of cylindrical inserts (Figure 44b) were used for experimental evaluation of different dynamic FFM protocols: 1) a cylindrical insert with 3 holes around the center to create a 3-stimuli signal; 2) a cylindrical insert with a single hole at the center for 1-stimuli signal; 3) a homogeneous cylindrical insert for a non-stimulus case. Lastly, a homogeneous elliptical phantom was employed for calibration (Figure 44a). Note that the contrast control as mentioned in section 2.5 was applied to create the 1- or 3-stimuli signals.

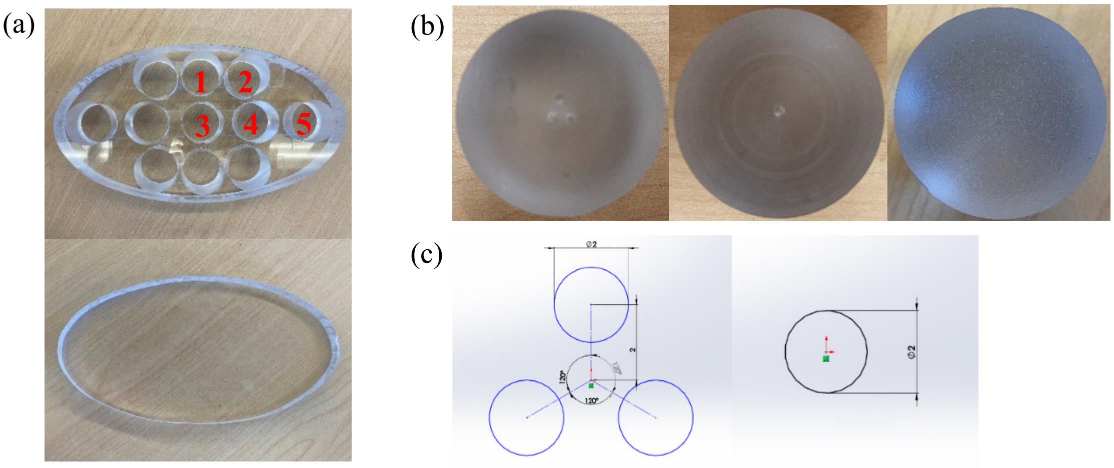

Figure 44: Phantoms being used in dynamic FFM studies. (a) Two elliptical PMMA phantoms being used during the experiment, one with 11 cylindrical vacancies and the other being homogeneous; (b) Three different kinds of cylindrical inserts, one with 3 holes around the center, another one with 1 hole at the center and the last one being homogeneous; (c) Spatial design of two kinds of stimuli. For 3-stimuli signal, each hole with 2mm diameter was uniformly distributed around the origin at radial distance of 2mm; for 1-stimuli signal, the hole with 2mm diameter is centered at the origin

For the elliptical phantom, phantom-specific FFM following three imaging objectives were designed:

1) *Minimum mean variance in FBP:* Spatial modulation is applied such that the mean variance over the object in an FBP reconstruction is minimized. Mathematically, assuming the line integral (*l*) of the phantom is known, the barebeam fluence field to be delivered is given by the following equation when α = 0.5 [25]:

$$I_0(u^*, \theta) = \frac{\exp[\alpha l(u^*, \theta)]}{\sum_\theta \exp[\alpha l(u^*, \theta)]} I_0^{tot} \qquad (13)$$

Here, I_0 denotes the target barebeam fluence, l denotes the line integrals of the object, and u^* denotes detector elements behind the phantom such that only fluence going through the object counts toward the total fluence, I_0^{tot}. To obtain l, a scout scan of the elliptical phantom was acquired under high exposure setting (0.4 mAs/frame).

2) *Static bowtie:* The dual-MAD filters were kept fixed at specific location, such that the spatial modulation resulted in nearly flattened fluence field along the major axis ($\theta = 0° \; or \; 180°$) behind the object. The TCM is similar in equation (1) but is scaled according to the fluence at the central detector. Mathematically, the barebeam fluence is given by the following equation when α = 1.0:

$$I_0(u^*, \theta) = \frac{\exp\left[\alpha l(u^*_{central}, \theta)\right]}{\sum_\theta \exp\left[\alpha l(u^*_{central}, \theta)\right]} I_0^{tot} \qquad (14)$$

3) *Task-driven:* The barebeam fluence is delivered following equation (13), but with α optimized to maximize the minimum of the stimuli detectability at all possible stimuli locations where the performance is quantified [26], as:

$$\underset{\Omega}{argmax} \underset{v}{min} \, d'_j(v; \Omega) \qquad (15)$$

Where the subscript j denotes the location-dependence, v denotes the volume of interest, and $\Omega = \{\Omega_A, \Omega_R\}$ includes the parameterization of FFM and regularization. Detectability is expressed as:

$$d'^2_j(\Omega_A, \Omega_R) = \frac{\left[\iiint W^2_{Taskj} T_j^2(\Omega_A, \Omega_R) df_x df_y df_z\right]^2}{\iiint S_j(\Omega_A, \Omega_R) T_j^2(\Omega_A, \Omega_R) W^2_{Taskj} df_x df_y df_z} \qquad (16)$$

Where T_j and S_j denotes the local MTF and NPS, and W_{Task} denotes the stimuli-detection task function.

3.2.3 Data Acquisition & Reconstruction

Three different phantom setups (Figure 44) were used in data acquisition: 1) all five stimuli locations were filled with 3-stimuli cylindrical inserts; 2) four 1-stimuli cylindrical inserts were filled at location 1, 2, 3 and 4; 3) all vacancies were filled with homogeneous inserts. In first two cases, the inserts were filled with potassium phosphate of contrast 200 HU to create the stimuli signal. The remaining locations in the 11-hole elliptical phantom were filled with homogeneous inserts.

Data was collected under low-exposure settings (0.08 mAs/frame), with the total barebeam fluence in all 3 protocols being matched. To collect the stimuli-present data, for each phantom setup in first two cases, the elliptical phantom was repeatedly scanned 3 times with the corresponding imaging protocol to provide additional noise realizations. The identical PMMA elliptical phantom was scanned twice (to reduce the noise) by using the same protocols to perform ring-artifact, beam-hardening and spectral corrections. Next, previous steps were repeated under the third phantom setup, except that it was scanned 8 times to produce more stimuli-absent images for the planned human observer study.

After data collection, the Penalized Likelihood (PL) approach was applied for reconstruction using 100 iterations of the SPS algorithm with 20 subsets, and a uniform quadratic roughness penalty with first-order neighborhood. The regularization strength β used in the 3-stimuli case was $10^{6.5}$; while in the 1-stimuli case it was $10^{6.7}$. A volume of $300 \times 600 \times 60$, 0.5mm isotropic cubic voxels was used for all reconstructions to cover the elliptical phantom. Finally, to remove the ring artifacts and perform spectral correction in both stimuli-present and stimuli-absent reconstructions, the average reconstruction of the homogeneous elliptical phantom was used (specifically, the reconstructions with inserts were divided by the homogeneous phantom and renormalized).

3.3 Human Observer Study

3.3.1 Data Preparation

To generate the best data for the human observer study, six phantom slices with an interspace of 1 mm (to prevent correlation on the vertical direction) were used across all FFM strategies and reconstructions. The stimuli-present ROIs were extracted, yielding 270 images in the 3-stimuli case (6 slices, 5 locations, 3 repeats and 3 imaging protocols) and 216 scans in the 1-stimuli case (only 4 locations). Note that there were 18 identical trials at each location under each imaging protocol, which can be used later to calculate Percent Correct (PC). Next, the stimuli-absent ROIs at the same locations were extracted, which rendered a background noise ROIs pool of size 48 at each insert's location. The ROIs were carefully selected such that the stimuli signal was always at the center of the rectangular ROI, and its orientation remained unchanged. The training data (to introduce observers to the detection task) was prepared in the same fashion but from the remaining slices, which contained 21 stimuli-present ROIs in total (7 from each imaging protocol).

3.3.2 Human Observer Study Design

A free-response 9AFC human observer study was designed based on an interactive MATLAB GUI. We target 20 untrained observers (scientists and engineers experienced with CT images) without prior knowledge about the stimuli to be invited to participate in this study. Prior to the real stimuli-detection test, observers will go through a supervised training process to familiar themselves with the appearance of stimuli under low-exposure settings and the software interface. For the relatively simple stimuli, these observers can be viewed as “sufficient” experts to perform such detection task.

The images will be displayed on a 13.5” monitor (Surface Laptop, Microsoft) with 2256×1504 display resolution. All studies will be conducted in the same dark room, with the lighting controlled to emulate a radiology reading room. During the test, a fixed window and level will be used for all images ([0.02, 0.023] for 3-stimuli detection task, [0.02 0.022] for 1-stimuli detection task) and no user change is allowed. The complete human observer study consists of 2 parts: 1) 3-stimuli detection task and 2) 1-stimuli detection task. In each part, the human observer will go through the training process and the real test, as shown in Figure 4: 1) compare the stimuli-present scan with the stimuli-absent one under high-exposure settings; 2) get familiar with the appearance of the stimuli in low-exposure settings by receiving a supervised training; 3) the real stimuli-detection test.

During the test, 9 scans will be present in each trial with randomized orders, with 8 of them randomly selected from the stimuli-absent ROIs pool and only 1 stimuli-present ROI at the same location. The observer is forced to choose one image with the highest probability to contain the stimuli signal; after the observer makes the choice, the 9 images will refresh and the next trial ensues. The observer is encouraged to take a small break whenever he/she feels exhausted. The 3-stimuli detection task and 1-stimuli detection task will be completed in one session, which lasts around 1.5 hours.

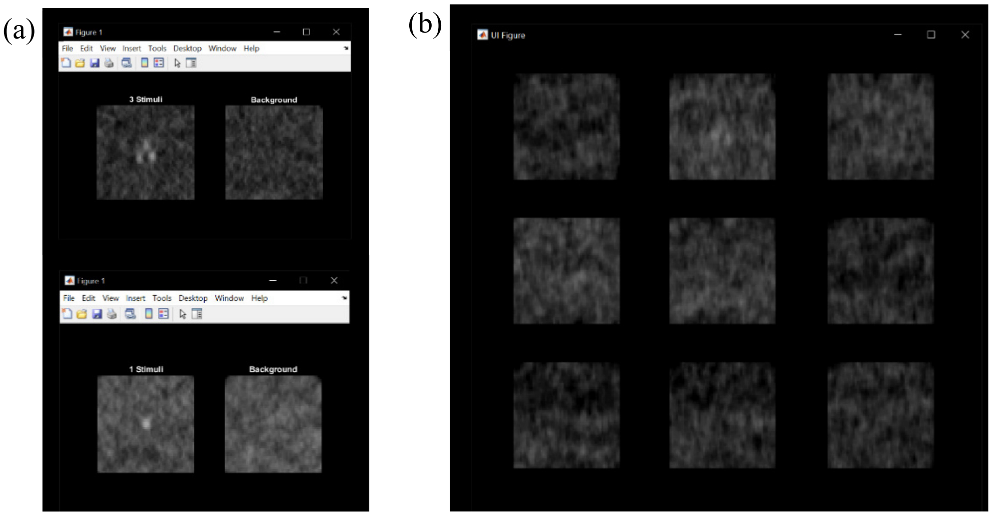

Figure 45: The user interface and different stages of the stimuli-detection task. (a) The first stage in each stimuli-detection task, which is the comparison between stimuli-present ground truth images and the stimuli-absent backgrounds; (b) The 9AFC user interface for both stimuli-detection tasks. Note that all images are displayed at the fixed window and level in each stimuli-detection task.

3.3.3 Statistical Analysis

The observer response at each trial is recorded as either 0 or 1 (wrong/correct choice). During the 9AFC test, the observer response, imaging protocol, observer index and trial index at each trial are recorded. Two approaches are adopted to perform the statistical analysis and to cross-validate the results: 1) based on the observer response recorded, the mixed-effects binary logistic regression is performed and 2) based on the PC calculated from the recorded observer response, the Fisher-Pittman exact test is carried out. For convenience, the following notations for imaging protocols and stimuli locations are used throughout the analysis:

$$P_1 - Conventional\ FFM\ with\ static\ bowtie\ filter$$

$$P_2 - Minimum\ mean\ variance\ in\ FBP\ Reconstruction\ dynamic\ FFM$$

$$P_3 - Task\ driven\ dynamic\ FFM$$

$$L_i (i = 1,2 \dots ,5) - Stimuli\ Location$$

For the mixed-effects binary logistic regression with categorical inputs, the imaging protocol and the stimuli location are considered as fixed effects, while the variation in human observer and trial index are considered as random effects. Eq.17 is used to evaluate different FFM imaging protocols locally:

$$logit\left(P_i \middle| L_j\right) = \beta_0 + \sum_{i \neq k, j \neq l} \beta_{ij} \cdot (P_i * L_j) + b + c \qquad (17)$$

Where:

$logit\left(P_i \middle| L_j\right)$ is the logit function value by using imaging protocol P_i at location L_j, which may be viewed as conditional terms based on different locations

β_0 is the reference logit function value chosen by using protocol P_k at location L_l

β_{ij} is the contrast between the logit function value of the reference and the one by using protocol P_i at location L_j

$(P_i * L_j)$ is a dummy variable of the interaction between imaging protocol and stimuli location as categorical inputs

$b \sim N(0, \sigma_b^2)$ and $c \sim N(0, \sigma_c^2)$ are random-effect intercepts modeling the variation in PC caused by different human observers and "repeated" trials

In mixed-effects binary logistic regression, the contrast β_{ij} represents the change of the success probability by using imaging protocol P_i at location L_j with respect to the reference, where the positive coefficient indicates the increase in probability and vice versa for the negative one. The pairwise comparison between different imaging protocols are performed by calculating all the contrasts β_{ij}, and the statistical significance is determined by p-value of the two-sided t-test for testing the null hypothesis $H_0\colon \beta_{ij} = 0$.

We will not only analyze the local performance of different imaging protocols, but also the comparisons between their global performance by estimating their marginal means as follows:

$$logit(P_i) = \sum_j w_j \cdot logit\left(P_i \middle| L_j\right) \qquad (18)$$

Where:

$logit\left(P_i \middle| L_j\right)$ is the logit function value by using imaging protocol P_i, which may be viewed as marginal terms grouped by imaging protocols

w_j is the weighting for each conditional term

Since the data in this 9AFC human observer test is balanced, the marginal term is just the average of conditional terms.

For the Fisher-Pittman exact test, both the global and local PC are computed, and they form the pairwise observations for each human observer. The following null hypothesis are tested globally and locally for comparing the mean PC among different imaging protocols:

$$H_{01}\colon \overline{PC}_{minimum\ variance\ in\ FBP} \geq \overline{PC}_{task-driven}$$

$$H_{02}\colon \overline{PC}_{static\ bowtie} \geq \overline{PC}_{task-driven}$$

$$H_{03}\colon \overline{PC}_{static\ bowtie} \geq \overline{PC}_{minimum\ variance\ in\ FBP}$$

At last, the Bonferroni multiple-comparison correction is applied to avoid spurious positives. Note that the significance level for the entire set of comparisons is chosen at 5% throughout the analysis.

3.4 Results

Since the human observer study is currently undergoing Institutional Review Board (IRB) reviewing process, no human observer data has been collected. In the future, we will conduct the observer study and evaluate the three FFM imaging protocols.

Conclusion

Procedural phantom development enables assessment of the ability of high-resolution CT to reproduce textures in reconstructions in a highly repeatable fashion. This methodology also has the following advantages: 1) a wide range of possible anatomical textures are permitted by a single general digital design, which facilitates the manufacturing process significantly; 2) The modular design allows the printed phantoms to be inserted into larger human body phantoms to take patient habitus into account; 3) Tissue contrast control can be achieved by immersing the phantoms in potassium phosphate or iodine solutions with varying concentrations. With increasing focus on task-based image quality and radiomics, such custom phantoms have the potential to play an increasing role in imaging performance assessments. In the future, we seek to improve the procedure way of phantom development to design more sophisticated texture features and to use more advanced 3D printers to achieve higher precision and printing quality. As for the dynamic FFM and the human observer study, we plan to conduct it as soon as the IRB review process is over and perform the statistical analysis to validate the efficacy of the dynamic FFM imaging protocol. In conclusion, both the procedural phantom generation and the human observer study are effective methods for CT image quality assessment.

Reference

[1] Kak, Avinash C., and Malcolm Slaney. *Principles of Computerized Tomographic Imaging*. Society for Industrial and Applied Mathematics, 2001.

[2] Prince, J. L., & Links, J. M. (2015). *Medical imaging signals and systems*. Boston: Prentice Hall. Page 188.

[3] Prince, J. L., & Links, J. M. (2015). *Medical imaging signals and systems*. Boston: Prentice Hall. Page 192.

[4] Fessler, Jeffrey A. *Statistical Image Reconstruction Methods for Transmission Tomography,* 2002. Page 6.

[5] Kak, Avinash C., and Malcolm Slaney. *Principles of Computerized Tomographic Imaging*. Society for Industrial and Applied Mathematics, 2001. Page 91

[6] L. A. Feldkamp, L. C. Davis, and J. W. Kress, "Practical cone-beam algorithm," J. Opt. Soc. Amer. A1(6), pp. 612–619, 1984.

[7] Fessler, Jeffrey A. *Statistical Image Reconstruction Methods for Transmission Tomography,* 2002. Page 8.

[8] Erdogan, H., & Fessler, J. A. (1999). Ordered subsets algorithms for transmission tomography. *Physics in Medicine and Biology*, *44*(11), 2835–2851. doi: 10.1088/0031-9155/44/11/311

[9] Wang, A. *et al.* (2015) "Accelerated statistical reconstruction for C-arm cone-beam CT using Nesterov's method". *Medical Physics,* 42(5), 2699-2708

[10] P. Lambin, E. Rios-Velazquez, R. Leijenaar, S. Carvalho, R.V. Stiphout, P. Granton, *et al.* *"*Radiomics: extracting more information from medical images using advance feature analysis", Eur J Cancer, 48 (4) (2012), pp. 441-446

[11] Kramer, R. et al. All about FAX: A female adult voXel phantom for Monte Carlo calculation in radiation protection dosimetry, Phys Med Biol, 49, 5203, 2004.

[12] Xu, X.G. and Shi, C. Preliminary development of a 4D anatomical model for Monte Carlo simulations, Monte Carlo 2005 Topical Meeting. The Monte Carlo Method:Versatility Unbounded In a Dynamic Computing World, Chattanooga, TN, April 17–21, 2005 2005.

[13] Rethy, Anna, et al. "Anthropomorphic Liver Phantom with Flow for Multimodal Image-Guided Liver Therapy Research and Training." *International Journal of Computer Assisted Radiology and Surgery*, vol. 13, no. 1, 2017, pp. 61–72., doi:10.1007/s11548-017-1669-3.

[14] [17] Hui Shi (2019). "The Use of 3D-printed Phantoms For Evaluating CT Image Quality". *Theses and Dissertations, Electronics (ETDs) – Graduate these, Johns Hopkins University.* http://jhir.library.jhu.edu/handle/1774.2/62312

[15] Hamzah, Hairul Hisham; Saiful, Arifin Shafiee; Aya, Abdalla; Patel, Bhavik Anil (2018). "3D printable conductive materials for the fabrication of electrochemical sensors: A mini review". *Electrochemistry Communications*. **96**: 27–371.

[16] Crivello, James V., and Elsa Reichmanis. "Photopolymer Materials and Processes for Advanced Technologies." Chemistry of Materials Chem. Mater. 26.1 (2014): 533. Print.

[18] Hui S. *et al.* (2019). “Performance assessment of texture reproduction in high-resolution CT”. *Proceedings Volume 11316, Medical Imaging 2020: Image Perception, Observer Performance, and Technology Assessment*;

https://doi.org/10.1117/12.2550579

[19] Gang, G. J., Mao, A., Wang, W., Siewerdsen, J. H., Mathews, A., Kawamoto, Stayman, J. W. (2019). Dynamic fluence field modulation in computed tomography using multiple aperture devices. *Physics in Medicine & Biology*, *64*(10), 105024. doi: 10.1088/1361-6560/ab155e

[20] Graham S A, Siewerdsen J H and Jaffray D A 2007 Intensity-modulated fluence patterns for task-specific imaging in cone-beam CT *Proc. SPIE* **6510** 651003

[21] J. Webster Stayman, Aswin Mathews, Wojciech Zbijewski, Grace Gang, Jeffrey Siewerdsen, Satomi Kawamoto, Ira Blevis, and Reuven Levinson "Fluence-field modulated x-ray CT using multiple aperture devices", Proc. SPIE 9783, Medical Imaging 2016: Physics of Medical Imaging, 97830X (22 March 2016); https://doi.org/10.1117/12.2214358

[22] M. D. Harpen, "A simple theorem relating noise and patient dose in computed tomography", *Med. Phys.*, vol. 26, no. 11, pp. 2231-2234, 1999, [online] Available: http://scitation.aip.org/content/aapm/journal/medphys/26/11/10.1118/1.598778.

[23] H. H. Barrett, K. J. Myers, C. Hoeschen, M. A. Kupinski, M. P. Little, "Task-based measures of image quality and their relation to radiation dose and patient risk", *Phys. Med. Biol.*, vol. 60, no. 2, pp. R1-R75, Jan. 2015, [online] Available: http://www.ncbi.nlm.nih.gov/pubmed/25564960.

[24] [26] Gang, G. J., Siewerdsen, J. H., & Stayman, J. W. (2017). Task-Driven Optimization of Fluence Field and Regularization for Model-Based Iterative Reconstruction in Computed Tomography. *IEEE Transactions on Medical Imaging*, *36*(12), 2424–2435. doi: 10.1109/tmi.2017.2763538

[25] M. D. Harpen, "A simple theorem relating noise and patient dose in computed tomography", *Med. Phys.*, vol. 26, no. 11, pp. 2231-2234, 1999, [online] Available: http://scitation.aip.org/content/aapm/journal/medphys/26/11/10.1118/1.598778

Junyuan Li

Email: jyli@jhu.edu
Personal website: https://jyli-personal.com/

EDUCATION

JOHNS HOPKINS UNIVERSITY, Baltimore, Maryland **Aug. 2018 – May 2020**
M.S.E in Biomedical Engineering
GPA: 4.0/4.0

(Purdue – SJTU 2+2 Dual Bachelor's Degree Honor Program)

PURDUE UNIVERSITY, West Lafayette, Indiana **Aug. 2016 – May 2018**
B.S.E in Mechanical Engineering
GPA: 4.0/4.0

SHANGHAI JIAOTONG UNIVERSITY (SJTU), Shanghai, China **Sep. 2014 - Jun. 2016**
B.E in Mechanical Engineering
GPA: 87.41/100

PUBLICATIONS & CONFERENCES

Journal Publications

1. Junyuan Li, Grace J. Gang, Craig K. Abbey, Webster J. Stayman. "Technical Notes: Evaluation of dynamic and static Fluence Field Modulation in low-dose CT scans", *Medical Physics (in preparation)*

Conference Proceedings & Presentations

1. **Junyuan Li**, Grace J. Gang, Michael Brehler, Hui Shi, Webster J. Stayman. "3D-Printed Textured Phantoms for Assessment of High Resolution CT", MEDICAL PHYSICS 46 (6), E209-E210. **Oral Presentation**, *American Association of Physicists in Medicine (AAPM) annual meeting 2019*, July 14 – 19, San Antonio, Texas

2. Hui Shi, Grace J. Gang, **Junyuan Li**, Eleni Liapi, Craig Abbey, and J. Webster Stayman. "Performance Assessment of Texture Reproduction in High-Resolution CT", Paper 11316-25. **Oral Presentation**, *SPIE Medical Imaging 2020*, Feb 15 – 20, Houston, Texas

Symposium Abstract & Presentations

1. Junyuan Li and Arezoo M. Ardekani, "Analytical Solution Of Microbes Interacting With Surfaces" (August 3, 2017). *The Summer Undergraduate Research Fellowship (SURF) Symposium.* Paper 23. https://docs.lib.purdue.edu/surf/2017/presentations/23

HONORS & AWARDS

Bottomley Undergraduate Research Scholarship, Purdue University	**Dec. 2017**
Summer Undergraduate Research Fellowship, Purdue University	**May 2017 – Aug. 2017**
Dean's list and Semester Honors, Purdue University	**All Semesters**

RESEARCH EXPERIENCE & INTERNSHIP

Dynamic Fluence Field Modulation (FFM) in X-ray CT by using Multiple Aperture Devices (MADs)

Apr. 2019 – Dec. 2019

School of Biomedical Engineering, Johns Hopkins University Advisor: Webster J. Stayman

This project aimed to validate the improvement of dynamic FFM integrated with task-driven optimization over conventional FFM with static bowtie filter by conducting a human observer study

- Systematically investigated the principles of MADs used in combination with cone-beam CT, including the device trajectory and tube current modulation (TCM) design, focal spot blur and spectral correction algorithms and the hardware implementation
- Studied the Penalized-likelihood reconstruction algorithm by using different penalty terms, such as total variation, quadratic penalty and Huber penalty; then performed parameter sweep to find the balance between noise reduction, resolution and edge preservation under varying imaging tasks
- Designed and conducted 9-Alternative Forced Choice (9AFC) human observer study of stimuli-detection task which mimics clinical diagnosis of microcalcification, then performed statistical analysis to validate the improvement of task-driven dynamic FFM over conventional FFM with static bowtie filter. Furthermore, analyzed the impact of the location, type, size and contrast level of stimuli on the observer performance

Development of 3D-printed phantoms for CT image quality assessment

Sep. 2018 – Mar. 2019

School of Biomedical Engineering, Johns Hopkins University Advisor: Webster J. Stayman

This project aimed to develop and fabricate anthropomorphic phantoms to evaluate the capability of the CT system to reliably reproduce the texture features

- Developed innovative, procedural routines for anatomical texture generation with 3D-printing technique, which was based on the idea of constrained voids packing within specified volumes
- Generated the phantoms simulating lung textures, and cross-evaluated the image quality of the reconstructions from Micro-CT, high-resolution cone-beam CT and helical CT

- Generated the phantoms mimicking trabecular bone textures and performed repeatability analysis
- Designed the anthropomorphic phantoms simulating the liver lesions caused by Hepatocellular Carcinoma (HCC) in different phases

On-chip Diagnostic of Malaria Viral Activity with Particle Image Velocimetry (PIV) technique

Sep. 2017 – Jan. 2018

School of Mechanical Engineering, Purdue University Advisor: Steven Wereley

This project aimed to quantify the Malaria Viral activity in the on-chip samples, which could further be incorporated into a portable device

- Recorded the Brownian motion of fluorescent nanoparticles in the on-chip Malaria DNA samples by using the PIV technique
- Performed auto-correlation and cross-correlation analysis in small interrogation windows between successive frames to measure the viscosity of the Malaria DNA solution
- Succeeded in calculating the viscosity of Malaria DNA solution under different temperatures or by using varying nanoparticle sizes to quantify the Malaria viral activity

Analytical and Numerical Solutions around Microbes Interacting with Surfaces

May 2017 – Aug. 2018

School of Mechanical Engineering, Purdue University Advisor: Arezoo Ardekani

This project aimed to numerically solve the velocity field around the self-propulsion microorganisms in bounded fluid domain

- Systematically investigated the Method of Regularized Stokeslets, which aims to de-singularize the forces exerted on the discretized points in fluid domain
- Developed several solvers to calculate and visualize the velocity field around the self-propulsion microorganisms (such as the beating cilia and the mammal sperms) in fluid domain with boundary condition of semi-infinite planar wall
- Validated the success of this numerical method by conducting error analysis with respect to analytical solution

SCHUNK GMBH & CO. KG (SHANGHAI), Shanghai, China **Jun. 2015 - Sep. 2015**

Internship

- Gained deep understanding of the design of zero-point holding system, including the sophisticated application of pneumatic and hydraulic control
- Investigated commercial zero-point holding systems in market and wrote technical report for comparison between SCHUNK's and its competitors' products

- Gained hands-on experience of dealing with real mechanisms by participating in field maintenance

EXTRACURRICULAR ACTIVITIES

International Friendship Program, Purdue University, West Lafayette, Indiana
Aug. 2016 – May 2018

Student Career Plan & Guidance Association, SJTU, China
Oct. 2014 - Jun. 2016

Graduation Ceremony Volunteer, SJTU, China
July 2015 & July 2016

Freshmen Enrollment Volunteer, SJTU, China
Sep. 2015

RELEVANT COURSES

Medical Imaging System, Imaging Instrumentations, Nonlinear Optimization I/II, Digital Image Processing, Medical Image Analysis, Signal and Systems, Mathematical Methods in Physics

SKILLS

Programming: C, C++, Python and MATLAB
Software: Solidworks, OpenSCAD
Hands-on experience of modeling and 3D-printing